IRIS AperTO

UNIVERSITÀ DEGLI STUDI DI TORINO

AperTO - Archivio Istituzionale Open Access dell'Università di Torino

Partial melting in the Higher Himalayan Crystallines of Eastern Nepal: the effect of decompression and implications for the “channel flow” model.

This is the author's manuscript

Original Citation:

Availability:

This version is available http://hdl.handle.net/2318/94464 since

Published version:

DOI:10.1093/petrology/egs009

Terms of use:

Open Access

Anyone can freely access the full text of works made available as "Open Access". Works made available under a Creative Commons license can be used according to the terms and conditions of said license. Use of all other works requires consent of the right holder (author or publisher) if not exempted from copyright protection by the applicable law.

(Article begins on next page)

23 August 2022

UNIVERSITÀ DEGLI STUDI DI TORINO

This is an author version of the contribution published on:
Questa è la versione dell'autore dell'opera:

Groppo C., Rolfo F. & Indares A. (2012). Partial melting in the Higher Himalayan Crystallines of Eastern Nepal: the effect of decompression and implications for the "channel flow" model. Journal of Petrology, 53, 1057-1088, doi: 10.1093/petrology/egs009

The definitive version is available at:
La versione definitiva è disponibile alla URL:
http://petrology.oxfordjournals.org/content/53/5/1057.full

Partial melting in the Higher Himalayan Crystallines of Eastern Nepal: the effect of decompression and implications for the "channel flow" model.

Chiara Groppo[1], Franco Rolfo[1,2] & Aphrodite Indares[3]

1 - Department of Mineralogical and Petrological Sciences, University of Torino, via Valperga Caluso 35, I-10125, Torino, Italy
2 - IGG – CNR, Via Valperga Caluso 35, I-10125, Torino, Italy
3 - Department of Earth Sciences, Memorial University of Newfoundland, St John's, NF, Canada A1B3X5

[*] **Corresponding author:**
Chiara Groppo
Phone: +39 011 6705106
Fax: +39 011 6705128
e-mail: chiara.groppo@unito.it

Short title: Partial melting in the Higher Himalayan Crystallines

Abstract

Partial melting of deep continental crust may occur during either prograde heating or decompression. Although the effect of temperature on crustal melting has been widely investigated, only few experimental studies addressed the question of the influence of pressure on crustal anatexis. In order to understand the influence of decreasing pressure on partial melting processes, the thermodynamic approach of isochemical phase diagrams has been applied on garnet-K-feldspar-kyanite-sillimanite anatectic gneisses (Barun Gneiss) from the Higher Himalayan Crystallines of eastern Nepal.

The main melt-producing reactions, the amount of melt produced during heating vs. decompression, and the effects of melt loss on the mineral assemblages and compositions have been investigated along four ideal P-T trajectories dominated by either heating or decompression. Resting on these results, the observed microstructures and measured mineral compositions of the Barun Gneiss have been interpreted in terms of melt-producing vs. melt-consuming reactions (e.g. growth of peritectic garnet with preserved "nanogranites" inclusions vs. microstructures related to back-reactions between solids and melt), and used to derive the metamorphic evolution of the studied samples. The P-T pseudosection modelling predicts that at least 15-20 vol% of melt was produced at peak P-T conditions through dehydration melting of both muscovite and biotite, and that melt production was mainly triggered by heating, with or without the combined effect of decompression. The preserved granulitic peak assemblage, however, is consistent with a significant loss of most of this melt.

The P-T evolution inferred for samples from different, strategically-located, structural levels of the Barun Gneiss, are consistent with the expectations of the "channel flow" model, including: (i) the clockwise shape of the P-T paths; (ii) the estimated P at peak-T (new data: 10 to 8 kbar at 800°C; model: 13 to 7 kbar at 800°C); (iii) the decreasing P structurally upward, which defines a "normal" metamorphic sequence, in contrast to the inverted metamorphic sequence occurring in the lowermost Main Central Thrust Zone; (iv) the nearly-isothermal exhumation of the structurally

lower sample, reflecting the progressive exhumation of rocks that have been entrained in the deep, high-T region of the channel, vs. the nearly isobaric heating of the structurally upper sample, reflecting the evolution of those rocks which flowed outwards with the underlying channel.

Key-words: “channel flow” model; decompression melting; Higher Himalayan Crystallines; Himalaya; partial melting

INTRODUCTION

Crustal anatexis is one of the most important processes responsible for the differentiation of the continental crust (e.g. Vielzeuf & Holloway, 1988; Brown, 1994; Vielzeuf & Montel, 1994; Brown & Rushmer, 2006) and for the genesis of granitic magmas (e.g. Thompson, 1982; Vielzeuf *et al.*, 1990; Clemens, 1990; 2006). The general interest in crustal anatexis has progressively increased during the last decades, also because partial melting deeply affects the rheology and geodynamic behaviour of the crust, thus playing a major role in the tectonic evolution of collision orogens (e.g. Vanderhaeghe, 2001; Whitney *et al.*, 2004).

In the deep continental crust, the generation of a significant melt fraction requires temperatures in excess of 800°C because rocks are dry (e.g. Clemens & Vielzeuf, 1987; Thompson & Connolly, 1995; Yardley & Valley, 1997). Under these conditions, dehydration melting involves the breakdown of muscovite and biotite in metasedimentary and granitic protoliths and of biotite and/or hornblende in amphibolites, respectively (e.g. Thompson, 1982; Clemens & Vielzeuf, 1987; Vielzeuf & Holloway, 1988; Patiño Douce & Johnston, 1991; Thompson & Connolly, 1995; White *et al.*, 2004; Clemens, 2006), yielding up to 10-50 vol% of water-undersaturated melt (e.g. Clemens & Vielzeuf, 1987; Vielzeuf & Holloway, 1988; Vielzeuf & Vidal, 1990; Brown & Rushmer, 2006). Furthermore, partial melting of deep continental crust may occur during either prograde heating or decompression (e.g. Whitney *et al.*, 2004 and references therein). The effects of temperature on crustal melting have been widely investigated using both experimental (e.g. Vielzeuf & Holloway, 1988; Patiño Douce & Johnston, 1991; Vielzeuf & Montel, 1994; Gardien *et al.*, 1995; Patiño Douce & Beard, 1996; Montel & Vielzeuf, 1997; Steven *et al.*, 1997; Patiño Douce & Harris, 1998; Pattison *et al.*, 2003) and forward modelling approaches (e.g. Spear *et al.* 1999; White & Powell, 2002; White *et al.*, 2004, 2007; Johnson *et al.*, 2008). Although fewer experimental studies directly addressed the question of the influence of pressure on crustal melting (Patiño Douce & Johnston, 1991; Vielzeuf & Montel, 1994; Vielzeuf & Schmidt, 2001; Auzenneau *et al.*, 2006), decompression melting was widely investigated using petrological models (e.g. Clemens & Vielzeuf, 1987; Vielzeuf & Schmidt, 2001; Thompson, 2001) and forward modelling approaches (e.g. Harris & Massey, 1994; Harris *et al.*, 2004; Streule *et al.*, 2010).

There is a general consensus in considering three major factors controlling the melt productivity in deep continental crust (e.g. Clemens & Vielzeuf, 1987): (i) the maximum temperature reached during metamorphism (T_{max}); (ii) the pressures experienced in the supra-*solidus* domain, and (iii) the mineralogy of the source rock, which in turn controls the initial amount of H_2O in the starting material. The effect of temperature on melt production is intuitive: the highest is T_{max}, the largest is the amount of melt produced, regardless from the source rock (e.g. Vielzeuf & Holloway, 1988; Patiño Douce & Johnston, 1991; Gardien *et al.*, 1995; Steven *et al.*, 1997; Patiño Douce & Harris, 1998). On the contrary, the effects of pressure on melt productivity are less intuitive and often vary as a function of the bulk composition of the protolith. In particular, although theoretical models generally predict that any given source rock will produce more melt at lower pressure because melts dissolve more H_2O at higher pressure (e.g. Clemens & Vielzeuf, 1987), the strong effect of pressure on melt fraction is often not borne out by experimental studies (e.g. Patiño Douce & Johnston, 1991; Patiño Douce & Beard, 1996; Steven *et al.*, 1997; Montel & Vielzeuf, 1997), which sometimes also suggest an opposite relation (i.e. the melt fraction decreases with decreasing P) (e.g. Gardien *et al.*, 1995; Auzennau *et al.*, 2006). Therefore, the effectiveness of decompression melting in the production of large amounts of melt in the deep crust is still far from being universally demonstrated.

An additional issue to be considered in the study of partial melting is the possibility for melt loss from the source rock, especially in tectonically active environments. Melt loss episodes during crustal anatexis at mid- to high-crustal depth have been suggested since 1970's (e.g. Fyfe, 1973; Powell & Downes, 1990; Sawyer, 1998) and have been initially investigated on the basis of geochemical and/or petrographic constraints (e.g. Sawyer, 1987; Barbey *et al.*, 1996; Sawyer *et al.*, 1999). However, quantitative modelling of the melt loss effects has been only recently attempted (White & Powell, 2002; Guernina & Sawyer, 2003; White *et al.*, 2004; Johnson *et al.*, 2008). These studies suggest that a substantial proportion of the melt produced during prograde and peak metamorphism should be lost from the source rock in order to preserve the coeval, granulite facies mineral assemblages (Brown, 2002, 2007; White & Powell, 2002; Guernina & Sawyer, 2003). Alternatively, if no melt loss occurs, the anhydrous granulitic assemblages are prone to extensive retrogression during cooling, and hydrous assemblages will develop through back reactions involving the crystallization of melt.

In order to contribute to this topical subject, this paper focuses on microstructures, mineral compositions and P-T evolution of garnet-K-feldspar-kyanite-sillimanite anatectic gneisses (Barun Gneiss) from the Higher Himalayan Crystallines of eastern Nepal. The main melt-producing (and melt-consuming) reactions, the amount of melt produced during heating vs. decompression, and the effects of melt loss on the mineral assemblages and compositions, have been investigated using the thermodynamic approach of isochemical phase diagrams. Several reasons make these Grt-Kfs-Ky-Sil anatectic gneisses an exceptional natural laboratory for investigating the influence of decreasing pressure on partial melting processes:

(i) Although preliminary thermobarometric studies (Pognante & Benna, 1993) and more recent P-T determinations (Streule *et al.*, 2010) suggest that Barun Gneiss experienced a nearly isothermal decompression from the kyanite to the sillimanite stability field, their P-T evolution is still poorly constrained. The main aim of this work is then to reconstruct, using the most recent petrological approaches, the P-T evolution of a still poorly investigated high-grade tectonometamorphic unit.

(ii) Barun Gneiss (and their laterally equivalent Kangchenjunga Gneiss and Darjeeling Gneiss; see Goscombe *et al.*, 2006 for a review) is an east–west-trending, 2-3 km thick, sequence of granulitic and migmatitic metasediments, laterally continuous for at least 200 km along the Himalayan chain, from eastern Nepal to Sikkim and Bhutan. Moreover, recent studies on the Namche Barwa syntaxis (Guilmette *et al.*, 2010), located at the easternmost margin of the Himalayan chain 1000 km east of the Barun Gneiss type locality, have shown the existence of very similar Grt-Kfs-Ky-Sil rocks. Therefore, these anatectic rocks represent a truly significant portion of the metamorphic core of the Himalaya. This study thus represents an opportunity for understanding similarities and differences between two distant sectors of the Himalayan chain, and for eventually demonstrating the existence of a HP-HT belt with similar characteristics through the whole eastern portion of the Himalayas.

(iii) Barun Gneiss is located in a key sector of the Himalayan chain (i.e. Higher Himalayan Crystallines), where many of the current geological models predicting the tectonic evolution of collisional orogens have been defined, such as the "channel-flow model" of Beaumont *et al.* (2001) and the "tectonic aneurism model" of Zeitler *et al.* (2001). Therefore, constraining the P-T evolution of the Barun Gneiss also provides the opportunity to test these models.

(iv) Medium- to high-pressure (i.e. kyanite-bearing) natural anatectic rocks have been considerably less investigated (e.g. Janak *et al.*, 1999; Harris *et al.*, 2004; Indares *et al.*, 2008; Guilmette *et*

al., 2010) than low pressure (i.e. sillimanite- and cordierite-bearing) migmatites. This paper will then contribute to the understanding of a complex process (i.e. the role of decompression on partial melting) at still poorly investigated P-T conditions (i.e. kyanite stability field), in the most prominent collision orogen on Earth (i.e. the Himalaya).

PARTIAL MELTING IN THE HIGHER HIMALAYAN CRYSTALLINES OF EASTERN NEPAL: GEOLOGICAL BACKGROUND

In the eastern Himalayan chain, partial melting is widely documented in the Higher Himalayan Crystallines (HHC) (Fig. 1) (e.g. Bordet, 1961; Brunel & Kienast, 1986; Lombardo *et al.*, 1993; Pognante & Benna, 1993; Swapp & Hollister, 1991; Davidson *et al.*, 1997; Neogi *et al.*, 1998; Goscombe & Hand, 2000; Grujic *et al.*, 2002; Daniel *et al.*, 2003; Dasgupta *et al.*, 2004; Harris *et al.*, 2004; Jessup *et al.*, 2008; Searle *et al.*, 2008; Imayama *et al.*, 2010; Streule *et al.*, 2010). In the framework of the crustal architecture proposed by Goscombe *et al.* (2006) for the Himalaya in eastern Nepal, which we will follow in this work, the HHC (Upper Plate of Goscombe *et al.*, 2006; see also Groppo *et al.*, 2009) is a high-grade, 5-6 km thick lithotectonic unit located at the higher structural levels of the Himalayan belt. The HHC is bounded at its base by the High Himal Thrust (HHT) bordering the structurally lower Main Central Thrust Zone (MCTZ), and at its top by the South Tibetan Detachment System (STDS) bordering the structurally higher Tethyan Sedimentary Series, which were responsible for reverse and normal movements respectively, between 22 and 11 Ma (e.g. Hodges *et al.*, 1992; Searle, 1999; Harrison *et al.*, 1999; Godin *et al.*, 2001, 2006; Catlos *et al.*, 2004; Kellet *et al.*, 2010).

The lower part of HHC is a 2-3 km thick sequence in which medium-P granulite-facies metasediments (Grt + Kfs + Ky + Sil + Pl + Qtz) are associated with large tabular bodies of granitic orthogneisses and crosscut by abundant concordant and discordant granitic dykes. Both metasediments and orthogneisses display evidence of medium- to low-P dehydration melting of micas. The high-grade migmatitic metasediments are known as Barun Gneiss in the Everest-Makalu region (Bordet, 1961; Brunel & Kienast, 1986; Lombardo *et al.*, 1993; Pognante & Benna, 1993), Jannu- Kangchenjunga Gneiss in the Kangchenjunga region of far east Nepal (Mohan *et al.*, 1989; Goscombe & Hand, 2000) and Darjeeling Gneiss in Sikkim (Dasgupta *et al.*, 2004; Harris *et al.*, 2004) and Bhutan (Swapp & Hollister, 1991; Grujic *et al.*, 2002; Daniel *et al.*, 2003). Granitic orthogneisses are defined as Namche Migmatite Orthogneiss in the Everest-Makalu region (Lombardo *et al.*, 1993). The upper part of the HHC consists of biotite paragneisses and micaschists (Black Gneiss in the Everest-Makalu region: Bordet, 1961; Yangma Paragneiss in the Kangchenjunga region: Goscombe *et al.*, 2006) hosting networks and lens-shaped bodies of two-micas and tourmaline-bearing leucogranites, which can be as thick as 1-2 km (Makalu, Baruntse) (Visonà & Lombardo, 2002).

Barun Gneiss

The P-T evolution of the Barun Gneiss in the Everest-Makalu region is still poorly known (e.g. Goscombe *et al.*, 2006). So far, it has been investigated in some detail by Pognante & Benna (1993), Goscombe & Hand (2000) and Streule *et al.* (2010) but their results are significantly different. Pognante & Benna (1993) studied the HHC in the Khumbu region and in the Arun and Barun Valleys (eastern Nepal). They recognised a metamorphic zonation in the Barun Gneiss, defined by a pressure decrease toward structurally upper levels; the metamorphic assemblages are of uniformly high grade but a progressive increase in the degrees of migmatization upward in the

sequence has been described. Pognante & Benna (1993) also reported the abundant occurrence of kyanite relics within garnet from the lower structural level of the Barun Gneiss. The P-T evolution of the Barun Gneiss has been constrained by these authors using conventional thermobarometry (i.e. Grt-Bt thermometer and Grt-Pl-Als-Qtz barometer). They proposed a P-T path characterized by a nearly isothermal decompression from the kyanite stability field (550-680°C, 8-10 kbar) to the sillimanite field (650-750°C, 5-7 kbar), followed by final cooling and decompression.

Goscombe & Hand (2000) obtained a quite different P-T evolution using the Average PT method combined with conventional thermobarometry. In contrast to Pognante & Benna (1993), these authors did not recognise kyanite relics in the Barun Gneiss assemblages, and thus restricted the prograde path to the sillimanite field. By considering the matrix assemblage Grt + Pl + Kfs + Qtz + Sil + Bt + Ilm ± Rt ± Crd of the uppermost levels of the Barun Gneiss, they constrained peak P-T conditions at 837±59°C, 6.7±1.0 kbar, followed by a nearly isobaric cooling down to <700°C. The P-T path they proposed, based on rare hercynite inclusions in garnet, consists of a counterclockwise P-T loop entirely comprised within the sillimanite field.

A more recent contribution is that of Streule *et al.* (2010), mostly devoted to the connection between the timing of high-grade metamorphism and leucogranite production in the upper structural levels of the HHC. With this aim in mind, they studied in detail the upper portion of the Barun Gneiss in the Barun Valley, using the Average PT method combined with qualitative pseudosection analysis. The P-T path they proposed is similar in shape to that proposed by Pognante & Benna (1993), although shifted to significantly lower P and T.

GRT-KFS-KY-SIL ANATECTIC BARUN GNEISSES: MICROSTRUCTURES AND MINERAL CHEMISTRY

The studied rocks outcrop along the Arun-Barun transect toward the Nepalese Makalu base camp, in the sector between Kauma to the south and Yangle Kharkha to the north across the Shipton La and Tu La Pokhri (Fig. 1). This is the type locality where the Barun Gneiss have been defined by Bordet (1961) and Lombardo *et al.* (1993), though these rocks have a peculiar petrography and are easily recognisable also elsewhere (e.g. the Khumbu, Arun-Mewa Khola and Kangchenjunga transects in eastern Nepal; Goscombe *et al.*, 2006; Groppo & Rolfo, 2010; Mosca *et al.*, 2010).

At the outcrop scale, the Barun Gneiss typically consists of millimetre to centimetre thick leucocratic quartzo-feldspathic domains alternating with millimetre dark biotite + plagioclase + sillimanite layers, which generally define a more or less continuous planar foliation (Fig. 2a, b). Two additional minerals are always present in the Barun Gneiss: (i) pink-red garnet, occurring as millimetric to centimetric porphyroblasts generally enveloped by the Bt+Pl+Sil foliation or occurring within the leucocratic domains (Fig. 2b), and (ii) kyanite, that always occurs as a relict phase generally corroded by plagioclase ± biotite. The amount of garnet and kyanite is strongly variable and kyanite is sometimes very rare: in this case it is not visible in the hand sample. Barun Gneiss are locally crosscut by decimetre thick granitic dykes both concordant and discordant with the foliation (Fig. 2a). Boudins and nodules of calc-silicate granofels consisting of diopside + plagioclase + quartz ± garnet ± scapolite are locally included in the Barun Gneisses and are enveloped by the regional foliation (Fig. 2c). About twenty five samples have been petrographically studied along the transect (see Table SM1 available as Supplementary Material, samples 07-14 to 07-40); among them, two Barun Gneiss samples have been selected and petrologically investigated in detail: sample 07-16 has been collected immediately north of Kauma, whereas sample 07-35 has been collected north of Mumbuk, very near to the Barun river. Both the samples have a pelitic

composition and plot in the shale and greywacke fields, respectively, according to the classification of Herron (1988) (Fig. SM1 available as Supplementary Material). These two samples have been chosen because they come from different, strategically-located structural levels within the Barun Gneiss (lower: 07-16; upper: 07-35) (Fig. 1); garnet and kyanite, are more abundant in sample 07-16 than in 07-35 (Fig. 3, 4, 5). Location of sample 07-35 roughly coincides with that of sample A81 described by Streule *et al.* (2010). However, their sample does not contain kyanite.

Structurally upward in the sequence, the Barun Gneiss is followed by a several hundred metres- thick sequence of Ca-silicate granofels and marbles and by cordierite-bearing ortho- and para- gneisses (Namche Migmatite orthogneiss of Lombardo *et al.*, 1993 and Black Gneiss of Bordet, 1961) (Table SM1, samples 07-24 to 07-31).

Sample 07-16

Petrography

Sample 07-16 shows a gneissic structure and mainly consists of quartz (37 vol%), plagioclase (21 vol%), K-feldspar (15 vol%), biotite (12 vol%), garnet (8 vol%), kyanite and sillimanite (7 vol%), accessory rutile rimmed by ilmenite and minor apatite. Two main domains may be recognised (Fig. 3a, 4a):

(i) coarse-grained leucocratic domains mainly consisting of quartz and K-feldspar. In these domains quartz forms ribbons parallel to the main foliation, often surrounded and/or partially corroded by K-feldspar (Fig. 4f). K-feldspar occurs as large aggregates of fine- to medium-grained crystals (Fig. 4f, 4i).

(ii) millimetric fine-grained mesocratic domains, consisting of biotite + plagioclase + sillimanite + quartz (Fig. 4a). These domains define a discontinuous foliation and partially replace the K-feldspar of the leucocratic domains (Fig. 4f). Quartz differs from that of the leucocratic domains because it is finer-grained and intimately associated to plagioclase and biotite (Fig. 4f). Prismatic sillimanite is generally rimmed by quartz (Fig. 4h, 4i).

Garnet and kyanite are randomly located in both the leucocratic and mesocratic domains (Fig. 3a, 4a). Garnet occurs as idioblastic porphyroblasts, up to few millimetres in diameter, generally enveloped by the discontinuous foliation (Fig. 4a). Garnet porphyroblasts consist of (Fig. 6a):

(i) a core, crowded with very small inclusions of quartz and graphite;

(ii) a mantle characterized by coarser inclusions of quartz ± rutile ± graphite. Quartz inclusions are locally surrounded by a thin film of plagioclase or, more rarely, K-feldspar: in this case, garnet shows crystal faces toward the inclusions (Fig. 4g, 4h).

(iii) a rim almost free of inclusions or locally including small and corroded kyanite crystals (Fig. 4b). Garnet is variably replaced at its rim by biotite + plagioclase symplectitic microstructures (Fig. 4c), and/or sillimanite + quartz aggregates (Fig. 4h).

Kyanite is abundant and clearly in disequilibrium with the stable mineral assemblage. It is locally corroded, always surrounded by a plagioclase ± biotite corona, and it is never in direct contact with either K-feldspar or quartz (Fig. 4d-f, 4i). Plagioclase surrounding kyanite is in turn corroded by sillimanite + quartz (Fig. 4i). Kyanite locally shows inclusions of quartz and biotite and it appears zoned in cathodoluminescence images (Fig. 4e).

Mineral chemistry

The three garnet domains, defined on the basis of microstructures, are also chemically distinct (Fig. 6a, Table 1 and see the Appendix for details on the analytical techniques), especially for X_{Ca}

[=Ca/(Ca+Mg+Mn+Fe)] that gradually decreases toward the rim (core: X_{Ca}=0.06-0.065; mantle: X_{Ca}=0.055-0.060; rim: X_{Ca}=0.040-0.050; outermost rim: X_{Ca}=0.025-0.030) (see also Fig. SM2-SM5, available as Supplementary Material). X_{Fe} [=Fe/(Fe+Mg)] is constant through the porphyroblasts, except for a gradual increase at the rim (core-mantle: X_{Fe}=0.73-0.75; outermost rim X_{Fe}=0.77-0.79). X_{Mn} [=Mn/(Ca+Mg+Mn+Fe)] slightly increases at the very outermost rim (X_{Mn}=0.04-0.05) (see also the Mn map in Fig. SM3), whereas it is almost homogeneous from core to mantle (X_{Mn}=0.025-0.035). It is underlined that in most garnet crystals the X_{Ca} chemical zoning closely corresponds to the microstructural zoning (see Fig. SM5, available as Supplementary Material).

Biotite and plagioclase in the fine-grained domains are chemically homogeneous (Table 1) with X_{Fe}=0.47-0.49 and Ti=0.22-0.23 a.p.f.u. in biotite, and X_{An}=0.19-0.22 in plagioclase. The biotite + plagioclase symplectites replacing garnet rim differ for the lower X_{Fe} and Ti contents of biotite (X_{Fe}=0.44-0.46; Ti=0.17-0.20 a.p.f.u.) and higher X_{An} content of plagioclase (X_{An}=0.24-0.25). K-feldspar shows a X_{Ab}=0.11-0.16.

Sample 07-35

Petrography

Sample 07-35 mainly consists of quartz (52 vol%), plagioclase (15 vol%), K-feldspar (14 vol%), biotite (9 vol%) and sillimanite (5 vol%). It has a gneissic structure defined by millimetric biotite + plagioclase ± quartz or prismatic sillimanite + quartz layers (Fig. 5a), which define a discontinuous foliation, alternating with plurimillimetric leucocratic layers consisting of quartz + K-feldspar + plagioclase (Fig. 3b, 5a). Garnet porphyroblasts (5 vol%) up to 5 mm in diameter are generally enveloped by the discontinuous foliation. Kyanite occurs as rare relics, always rimmed by a thick plagioclase corona (Fig. 5d); rutile is rimmed by ilmenite, and apatite is locally abundant. Minor graphite flakes are also present.

In the leucocratic layers, quartz, which occurs as coarse-grained elongated ribbons, and, locally plagioclase, show corroded rims against K-feldspar (Fig. 5b, 5e-f). In contrast, K-feldspar is partly replaced by plagioclase with intergrowths of quartz (myrmekite structures) (Fig. 5c) in contact with the biotite-bearing layers.

Garnet porphyroblasts have a spongy appearance and are crowded with different types of inclusions (Fig. 5a, 5g). In the inner portion of garnet porphyroblasts, very small inclusions (up to 20 microns in diameter) may be observed. Under optical microscope, they show birefringence but are too small for a more detailed characterization. When observed with the SEM, these inclusions show a negative-crystal shape and are clearly polyphasic (Fig. 5l), mainly consisting of quartz, biotite, K-feldspar and albitic plagioclase in different proportions, and do not connect with the matrix through fractures. At the garnet rim (Fig. 5g), inclusions are coarse-grained and polymineralic and mainly consist of rounded quartz and/or corroded biotite surrounded by a thin film or shell of plagioclase; garnet shows crystal faces toward plagioclase (Fig. 5h-i). Some garnet rims also contain apatite inclusions, and, rarely, sillimanite is also included in outer garnet rims (Fig. 5a). Biotite ± plagioclase locally replace garnet at its rim.

Mineral chemistry

Garnet in this sample is chemically heterogeneous (Table 1). Some garnet porphyroblasts are weakly zoned, with the core crowded of very small polyphase inclusions slightly enriched in X_{Ca} with respect to the rim with the large polymineralic inclusions (core: X_{Ca}=0.050; rim: X_{Ca}=0.040-0.045; Fig. 6b). However at the rims of garnet porphyroblasts with apatite inclusions, this zoning

pattern is complicated by a patchy, sharp and discontinuous X_{Ca} increase (up to X_{Ca}=0.19) (see also Fig. SM2-SM6-SM7, available as Supplementary Material). The outermost rim of most garnets is characterized by X_{Ca}=0.030-0.035. X_{Fe} profiles are generally flat (X_{Fe}=0.74-0.75) in garnet cores (Fig. 5b) but X_{Fe} increases (up to X_{Fe}=0.80-0.84) at the rims. X_{Mn} slightly increases at the very outermost rim (X_{Mn}=0.025-0.035) (see also the Mn map in Fig. SM4), whereas it is almost homogeneous from core to rim (X_{Mn}=0.010-0.020).

Plagioclase and biotite in the matrix are chemically homogeneous (Table 1), with X_{Fe}=0.49-0.52 and Ti=0.25-0.29 a.p.f.u. in biotite, and X_{An}=0.25-0.28 in plagioclase. In the large polymineralic inclusions in garnet, the corroded biotite flakes are depleted in both Fe and Ti (X_{Fe}=0.29-0.35; Ti=0.05-0.14), whereas plagioclase is enriched in Ca, with the highest anorthite content (X_{An}=0.57-0.58) corresponding to the Ca-enriched zones of garnet (see Fig. SM8, available as Supplementary Material). K-feldspar shows a X_{Ab}=0.12-0.18.

PHASE EQUILIBRIA MODELLING OF GRT-KFS-KY-SIL ANATECTIC BARUN GNEISSES

Two different P-T pseudosections have been calculated for each sample, representing two end-member cases and based on the inference that the measured bulk compositions may be melt-depleted: (i) a first set of pseudosections was calculated using the measured bulk-rock composition (case I: 07-16a and 07-35a, Table 2 and Fig. 7); and (ii) a second set of pseudosection was calculated using the bulk compositions obtained from one-step melt re-integration (case II: 07-16b and 07-35b, Table 2 and Fig. 8). The composition of the added melt was calculated at P-T conditions of 790°C, 11 kbar, which represent the hypothetical conditions at which melt was lost. In order to create the melt-reintegrated compositions (07-16b and 07-35b in Table 2), a specific amount of this melt was added to the measured bulk compositions. This specific amount of added melt (15 mol% for sample 07-16 and 16 mol% for sample 07-35) is sufficient to displace the *solidus* to H_2O saturated conditions, and therefore to maximize the amount of mica present before melting (see Indares *et al*. 2008). In natural systems it is not possible to know the exact melt loss history (i.e. the total amount and composition of missing melt, and the number of episodes of melt loss) and therefore the exact missing melt cannot be added back to reconstruct the real sub-*solidus* protolith. However forward modelling has shown that different scenarios of melt loss do not change significantly the supra-*solidus* topologies (White & Powell, 2002; Powell *et al*., 2005) and the approach used here is useful to investigate the extended supra-*solidus* domain-topologies before melt loss. Details on the estimate of the bulk compositions for both case I and case II and on the pseudosection modelling are given in the Appendix.

General topologies of the P-T pseudosections: melt-producing reactions during heating vs. decompression

Fig. 7 and 8 report the P-T pseudosections calculated for sample 07-16 in case I (actually measured bulk compositions 07-16a) and case II (melt-reintegrated composition 07-16b), respectively. The P-T pseudosections modelled for sample 07-35 show a very similar topology both in case I and in case II (compare the following Fig. 9 and 10), therefore for practical purposes, phase assemblages and melt-producing reactions will be qualitatively discussed using the P-T pseudosections obtained for sample 07-16. Changes in mineral assemblages and compositions are investigated along four ideal P-T trajectories crossing into the stability field of melt + garnet + biotite + K-feldspar + plagioclase + Al-silicate + quartz + rutile (hereafter referred to as field A), along which dehydration

melting of biotite occurs (see below): (1) isobaric heating (ΔT=140°C); (2) heating decompression (ΔT=100°C, ΔP=-7 kbar); (3) isothermal decompression (ΔP=-7 kbar); (4) cooling decompression (ΔT=-100°C, ΔP=-7 kbar). In order to compare more easily the melt productivity along the four different trajectories, the peak-T reached by paths 1 and 2 has been set at 880°C and the minimum P reached along paths 2, 3 and 4 has been set at 7 kbar.

For the melt-depleted case I, the *solidus* of the system is fluid-absent and it is located at T >775°C for P <12 kbar, whereas it coincides with the white mica-out reaction at P >12 kbar. In the field A, most of the modelled mineral isomodes are nearly parallel to the *solidus* (Fig. 7a), and the maximum amount of melt produced in this field is about 9 vol%, at its high-T limit. For the melt re-integrated case II, the wet *solidus* of the system is located at 650°C<T<690°C for P>5 kbar, and melt amounts higher than 30 vol% are modelled at the high-T side of field A (Fig. 8a). The topologies of the two pseudosections for case I and case II are very similar for T>790°C (i.e. at T above that at which melt was added), whereas they differ considerably for T<790°C.

Isobaric heating (path 1)

The first significant melt-producing reaction encountered along the isobaric heating path 1 is the reaction R1 (Fig. 7, 8), which coincides with the dehydration melting of muscovite as discussed by Le Breton & Thompson (1988) and Vielzeuf & Holloway (1988). This reaction is responsible for a significant increase in melt, K-feldspar and Al-silicate fractions, according to:

Wm + Qtz + Pl = L + Kfs + Als (R1).

The disappearance of white mica by R1 marks the entrance to the field A (Fig. 7, 8). With increasing T in this field, dehydration melting of biotite occurs according to the general reaction:

Qtz + Als + Bt + Pl = L + Grt + Kfs (R2),

which has been widely investigated by experimental petrologists (e.g. Vielzeuf & Holloway, 1988; Patiño Douce & Johnston, 1991; Vielzeuf & Montel, 1994; Vielzeuf & Schmidt, 2001).

The continuous reaction R2 is responsible for a modal increase of melt, K-feldspar and garnet (Fig. 7a, 8a). The total amount of melt produced at the high-T side of field A (T≈830°C) by isobaric heating along path 1 is 6 vol% (melt-depleted case I) and 23 vol% (melt-reintegrated case II) at P≈12 kbar.

When the Bt-out boundary is crossed, garnet and K-feldspar begin to be slightly consumed (Fig. 7a, 8a), according to the general melt-producing reaction R3 (Spear *et al.*, 1999):

Grt + Kfs + Ky + Pl + Qtz = L (R3),

which accounts for further production of melt up to a total of ca. 8 vol% (case I) and 27 vol% (case II) at T≈880°C.

Decompression (paths 2, 3 and 4)

Whether melt will be produced or consumed along any of these P-T trajectories depends on how this trajectory crosses the melt isomodes on the P-T pseudosection (Fig. 7, 8). In the P-T field A, these isopleths have subvertical negative (case I) to positive (case II) slope with increasing dP/dT towards higher T-lower P. The general increase of melt proportion with decreasing pressure observed in the case II pseudosection is linked to the decrease of the solubility of water in the melt with pressure (decompression melting: Clemens & Vielzeuf, 1987; Montel & Vielzeuf, 1997).

Path 2 (heating decompression) - During decompression along the P-T trajectory 2, the melt-producing reactions are the same discussed for trajectory 1 (i.e. reactions R1, R2 and R3). Within field A, melt together with garnet and K-feldspar is continuously produced at the expense of biotite, plagioclase, quartz and Al-silicate (Fig. 7a, 8a). The total amount of melt produced along

trajectory 2 strongly depends from the ΔT and ΔP: for both the melt-depleted and melt-reintegrated cases I and II, the melt productivity increases with increasing T and decreasing P, up to ca. 12 vol% (case I) and 40 vol% (case II) at T≈880°C and P≈7 kbar, respectively.

Path 3 (isothermal decompression) - Along the isothermal decompression path 3, the melt-producing reaction R1 is crossed in both case I and case II, but upon entering field A the system behaviour is different for the two end-member cases I and II. In the melt-depleted case I, the bulk composition is considerably depleted in the H_2O component. In this case no melt is produced by decompression within field A, as the melt isomodes have subvertical to negative slope, nearly parallel to the P-T trajectory (Fig. 7a). In the melt-reintegrated case (case II), the melt fraction increases during decompression up to a total amount of 23 vol% at 7 kbar (Fig. 8a). Modelling of trajectory 3 clearly shows that, at pressures below the white mica breakdown (reaction R1), decompression melting can occur at constant T only if melt is not extracted from its source (case II) and even in this case the amount of melt strictly produced by biotite de-hydration melting (reaction R2) is very low.

Path 4 (cooling decompression) - Path 4 models exhumation from high- to mid-crustal depths accompanied by cooling. In this case, melt progressively crystallizes during decompression because this trajectory crosses the isomodes of melt towards a lower melt fraction (Fig. 7a, 8a). In addition, the distribution of mineral isomodes show that garnet, K-feldspar and melt are consumed, whereas plagioclase, biotite, quartz and Al-silicate are produced along this P-T path, both in case I and in case II. Due to the different position of the *solidus*, the resulting assemblage at 740°C, 7 kbar is different for the two end-member cases I and II. For case I, the modelled trajectory crosses the *solidus* (Fig. 7a), resulting in the assemblage Qtz+Pl+Kfs+Bt+Grt+Als+Rt. For case II, the P-T path 4 does not cross the *solidus* (Fig. 8a): therefore, melt is still stable at 740°C, 7 kbar (Qtz+Pl+Kfs+Bt+Grt+Als+Rt+L).

The behaviour of garnet and Al-silicates during heating vs. decompression

As shown by the pseudosection modelling, garnet is alternatively produced or consumed through the continuous reaction R2 (or its reverse) depending on the P-T trajectory followed by the sample (Fig. 7a, 8a and Fig. SM9). Fig. SM9 shows how garnet composition (in term of X_{Ca}) varies along the four ideal P-T paths. Because of the slow diffusivity of Ca in garnet, the trend of X_{Ca} growth zoning (if not the absolute growth composition) is likely to be preserved to some extent (Spear & Florence, 1992; Caddick *et al*., 2010). It is thus evident that:

(i) garnet grows during heating along trajectory 1, up to the high-T side of field A; during decompression it grows only along trajectory 2, up to the disappearance of biotite. In all the cases, garnet growth is associated to the progressive consumption of quartz, biotite, plagioclase and Al-silicate and to the production of melt (Fig. 7a, 8a). Therefore we would expect that: (a) the reactant phases, if included in garnet, would be corroded, and (b) garnet would show crystal faces against inclusions of former melt (Vernon & Collins, 1988).

(ii) if garnet grows during decompression, it should preserve a growth zoning characterized by a significant decrease in X_{Ca} toward the rim (Fig. 7b, 8b and SM9). Any other zoning pattern cannot be explained by garnet growth during decompression. A X_{Ca} decrease toward the rim also characterizes garnet growing during heating (path 1), but in this case the zoning pattern is significantly less pronounced (Fig. SM9). This is also consistent with the experimental results which predict that the grossular content of peritectic garnet is strongly P-dependent (e.g.

Vielzeuf & Montel, 1994; Patiño Douce & Beard, 1996; Montel & Vielzeuf, 1997; Auzennau *et al.*, 2006).

As concerning the Al-silicates, Fig. SM9 shows that during nearly isobaric heating (path 1), the Al-silicate is a peritectic product resulting from the white mica breakdown (reaction R1), but it is a reactant in the following biotite dehydration melting reaction R2. This behaviour is the same along the decompression-dominated paths 2 and 3. Conversely, Al-silicate is a product of melt-consuming reactions along path 4. This implies that in a natural sample, if the Al-silicate appears corroded by former melt, the sample should have experienced nearly isobaric heating and/or decompression associated with heating. Conversely, if the Al-silicate replaces a peritectic phase such as garnet, the sample should have experienced melt crystallization during cooling.

RESULTS

Interpretation of the microstructures in samples 07-16 and 07-35

The microstructures observed in samples 07-16 and 07-35 provide evidence of melt-producing or melt-consuming reactions and may be interpreted in terms of the ideal P-T trajectories previously discussed (Fig. 11). In addition, the overall mineralogy of the samples (Qtz+Pl+Ksp+Grt+Als+Bt) in conjunction with the evidence for former melt discussed below, indicates that the metamorphic peak was reached in field A.

Sample 07-16:

(i) Plagioclase and K-feldspar films around quartz inclusions in the garnet mantle (Fig. 4g-h) may be interpreted as pseudomorphs of liquid-filled pores as defined by Holness & Clemens (1999) and Holness & Sawyer (2008) and suggest that the garnet mantle grew during melting. In addition, the presence of corroded kyanite in the garnet rim suggests that garnet rim grew at the expense of kyanite. These microstructures together with the regular X_{Ca} decrease from garnet core to rim (Fig. 6a) can be explained by the isobaric heating path 1 or by the heating decompression path 2 within field A (Fig. SM9) (i.e. garnet mantle and rim are peritectic). The same trajectories can also explain quartz ribbons partially corroded by K-feldspar in the coarse grained leucocratic domains (Fig. 4f) (i.e. quartz is a reactant and K-feldspar is a product).

(ii) Biotite ± plagioclase symplectites locally observed at the rim of porphyroblastic garnet (Fig. 4c) are consistent with back-reactions involving melt crystallization (e.g. Waters, 2001; Cenki *et al.*, 2002; Kriegsman & Álvarez-Valero, 2010). In addition, garnet rim partially corroded by sillimanite + quartz (Fig. 4h) are consistent with melt crystallization in the sillimanite stability field, along a path that cuts the sillimanite isomodes towards increasing values (i.e. path 4; Fig. SM9).

(iii) The interpretation of the plagioclase ± biotite corona partially replacing kyanite (Fig. 4d-f, 5i) is quite complex. Plagioclase coronas around kyanite in similar granulitic rocks have been described and modelled by Tajčmanová *et al.* (2007) and Štipská *et al.* (2010) as the product of a diffusion controlled solid state process in the absence of melt. Plagioclase ± biotite coronas occurring in the studied sample 07-16 differ from those described by Tajčmanová *et al.* (2007) and Štipská *et al.* (2010) because kyanite shows an embayed shape (Fig. 5d, e). For this reason, our preferred interpretation is that kyanite was first corroded by melt according to a melt-producing reaction such as R2, and that the plagioclase ± biotite corona developed later, during melt crystallisation at lower pressure, by a mechanism comparable to that proposed by Štipská *et al.* (2010), but in the presence of melt (see also

Guilmette *et al.*, 2010). In addition, the plagioclase ± biotite corona around kyanite is locally corroded by sillimanite + quartz (Fig. 4i), thus suggesting that it formed before the sillimanite growth.

Sample 07-35:

(i) The very small polyphase inclusions in garnet core are interpreted as "nanogranites" according to the definition of Cesare *et al*. (2009). In addition to the microstructural and mineralogical data previously discussed, further evidence that they represent crystallized melt inclusions is given by preliminary chemical data obtained by re-homogenizing inclusions of this type from a sample (07-19) collected very closely to sample 07-35 (see Table SM1 and Fig. 1) (Ferrero *et al*., in press). The analysed nanogranites show a leucogranitic and peraluminous melt composition (SiO_2 ~ 74 wt%, Al_2O_3 ~ 13 wt%, FeO ~ 2.5 wt%, MgO ~ 0.5 wt%, CaO ~ 0.85, Na_2O ~ 2 wt%, K_2O ~ 5 wt%) (Ferrero *et al*., in press), consistent with the results of partial melting experiments on metapelites and metagraywackes.

(ii) The discovery (for the first time in the Himalaya) of nanogranites in the core of garnet porphyroblasts (Fig. 5l) is a clear evidence that garnet core grew during partial melting. In addition, plagioclase films or shells surrounding corroded quartz and biotite in the large polymineralic inclusions within garnet rims (Fig. 5h-i) may be interpreted as pseudomorphs of liquid-filled pores (e.g. Holness & Clemens, 1999; Holness & Sawyer, 2008). This interpretation is supported by the cuspate shapes of plagioclase against the consumed phases and by the crystal faces of garnet against plagioclase, and suggests that also the garnet rims grew during partial melting, at the expense of quartz and biotite (i.e. the whole garnet is peritectic). The microstructures described above, as well as the weak X_{Ca} decrease from garnet core to rim are consistent with garnet growth along paths 1 and 2. Furthermore, the presence of sillimanite inclusions in the garnet rim (Fig. 5a) suggests that garnet rims grew in the sillimanite stability field (i.e. sillimanite should has been already present before the growth of garnet rim).

(iii) However, the Ca-enriched zones in garnet rims with apatite inclusions (Fig. 3b) cannot be explained by any of the paths considered here. The discontinuous and sharp nature of this patchy zoning, together with the presence of Ca-rich plagioclase (with respect to plagioclase elsewhere; see also Fig. SM8, available as Supplementary Material) included in these rims is suggestive of a local change in the effective bulk composition. In other words, it is likely that during a certain step of the peritectic garnet growth, Ca increased locally in some rock domains. Ca-enriched domains in garnet with apatite inclusions may be common in kyanite-bearing anatectic rocks and are inferred to be related to apatite dissolution during partial melting at high pressure (Indares *et al.*, 2008; Groppo *et al.*, 2010 and Guilmette *et al.*, 2010). Apatite represents a significant reservoir of Ca and it has been experimentally demonstrated that its dissolution is enhanced in peraluminous melts such as those derived from the initial stages of metapelite anatexis (Wolf & London, 1994).

(iv) Plagioclase + quartz myrmekitic structures replacing K-feldspar in the leucocratic domains (Fig. 5c) suggest that during the final stages of the metamorphic evolution registered by the studied rock, K-feldspar was a reactant, whereas plagioclase and quartz were products. These microstructures are consistent with paths 3 and 4.

P-T constraints using the P-T pseudosections

Measured vs. melt-reintegrated bulk compositions

The studied samples do not show any evidence of late hydration/retrogression due to the late circulation of fluids, therefore the observed assemblages (in both qualitative and quantitative terms) represent the assemblages stable at the fluid-absent *solidus*, i.e. during the crystallization of the last fraction of melt. This is because at the fluid-absent *solidus* all the H_2O of the system was fixed in hydrous minerals (i.e. biotite) and reactions cannot had occurred unless some water was introduced in the system from the outside. As a consequence, the actually measured bulk rock compositions can be used to model the P-T conditions of melt crystallization. Furthermore, because it is unlikely that melt was extracted from the system during cooling/crystallization, the measured bulk rock compositions are also suitable to model the whole retrograde evolution of the studied samples, i.e. from peak P-T conditions to the *solidus* (see Indares *et al*., 2008 for details). Therefore, the P-T pseudosections calculated using the measured bulk-rock composition (case I: 07-16a and 07-35a, Table 2 and Fig. 7), was used to constrain the P-T evolution from peak temperatures to the complete crystallization of the melt. In contrast, the melt-reintegrated pseudosections (case II: 07-16b and 07-35b, Table 2 and Fig. 8) were used to evaluate the prograde evolution of the studied samples.

The modelled modal proportions of each phase have been used to check the consistency between the pseudosections and the observed mineral assemblages (Table 3), which correspond to the mineral assemblages present during final melt crystallization (i.e. at the *solidus*) (e.g. Indares *et al*., 2008; Guilmette *et al*., 2010).

The possible effects of bulk rock fractionation due to garnet growth have not been considered in the modelling, because previous studies on similar anatectic rocks (e.g. Marmo *et al*., 2002; Štípská & Powell, 2005; Tinkham & Ghent, 2005; Indares *et al*., 2008) have shown that these effects are negligible, especially if the garnet modal amount is low, as in the studied samples (see also Fig. SM2, showing that the modal amount of garnet cores in sample 07-16 is very low).

Strategy for constraining P-T conditions

First order constraints on the P-T range of the thermal peak are provided by the location of the stability field of the peak assemblage melt + garnet + biotite + K-feldspar + plagioclase + Al-silicate + quartz + rutile (field A) on the pseudosections. Further information on the P-T evolution of the studied samples are provided by both microstructural observations and garnet minero-chemical data.

Microstructures - Microstructural constraints are mainly represented by the type of aluminosilicate included in garnet rim, and they will be discussed in the following sections.

Garnet composition and zoning - Due to the slow diffusivity of Ca in garnet, the X_{Ca} zoning trend observed in garnet from both samples (Fig. 6 and Fig. SM3-SM4-SM5-SM6, available as Supplementary Material) likely represents, to some extent, preserved growth zoning (e.g. Spear *et al*., 1990; Kohn *et al*., 1997; O'Brien, 1997; O'Brien *et al*., 1997; Spear *et al*., 1999; Štípská & Powell, 2005; Hollis *et al*., 2006; Indares *et al*., 2008) and it has been therefore used to refine the P-T constraints obtained on microstructural basis. It has been in fact recently emphasized (Caddick *et al*., 2010) that, although significant modification of the original absolute growth compositions generally occurs at T > 750°C, the trends of prograde elemental zoning in garnet is generally preserved up to relatively high temperature, especially if garnet crystals are > 1 mm in diameter, as in both the studied samples.

Exception is the steep decrease in X_{Ca} observed at the outermost garnet rims (< 100 μm wide), which is inferred to represent diffusion controlled retrograde zoning, as also suggested by the correspondent X_{Mn} increase (Fig. SM3-SM4 and Fig. SM5-SM6, available as Supplementary Material). The X_{Ca} of the outermost rims is likely due to retrograde net transfer reactions, which in

anatectic rocks usually end when melt solidifies (because retrograde reactions are much slower in the absence of melt or fluid; e.g. Guiraud *et al.*, 2001, White & Powell, 2002). Therefore, the intersection of the X_{Ca} isopleths at the outermost garnet rim and the *solidus* can be inferred to represent the conditions of melt crystallization. On the contrary, the uniform Fe/(Fe+Mg) ratio (X_{Fe}) observed in the garnet cores and mantles for both samples (Fig. 6) is typical of diffusional homogenization at high temperatures, which results in the obliteration of Fe-Mg growth zoning. Since diffusional homogenisation of X_{Fe} may continue during early stages of cooling (Spear, 1991), the X_{Fe} of the garnet core provides minimum T constraints to the P-T conditions of the thermal peak. In order to discuss the possibility that peak T conditions reached by the studied samples were higher than those actually suggested by garnet X_{Fe} isopleths, alternative P-T paths have been shown and discussed in Fig. 9 and 10 (dashed lines). Finally, the increase in X_{Fe} toward the outermost garnet rim represents diffusion-controlled retrograde zoning promoted by exchange of Fe-Mg between garnet rims and biotite during cooling (e.g. Florence & Spear, 1991; Spear, 1991), possibly continuing at sub-*solidus* conditions.

For sample 07-35, in which garnet porphyroblasts locally show a patchy and discontinuous X_{Ca} zoning (Fig. 3b and Fig. SM2), the Ca-enriched zones of garnet have not been considered in the modelling because they are likely related to a local change in the effective bulk composition (see the previous discussion). Therefore, the P-T conditions of garnet growth have been constrained using compositional parameters of garnet porphyroblasts devoid of patchy zoning.

Peak-to-retrograde P-T evolution

In the P-T pseudosections modelled for samples 07-16 and 07-35 using the actually measured bulk rock compositions (07-16a and 07-35a, Table 2) the peak assemblage melt + garnet + biotite + K-feldspar + plagioclase + Al-silicate + quartz + rutile is modelled by the field A (Fig. 9a and 10a) located between the *solidus* and the biotite-out curve. In this field, most of the mineral isomodes modelled for all the phases are nearly parallel to the *solidus* (Fig. SM10 and SM12) and, in particular, the mineral proportions calculated at the *solidus* are in good agreement with the observed modal amounts of each phase (Table 3), thus confirming the consistency of the modelling.

Conditions of melt crystallization are constrained by the intersection between the X_{Ca} isopleths of the garnet outermost rim (07-16: X_{Ca}=0.025-0.030; 07-35: X_{Ca}=0.030-0.035) and the *solidus* at 790-800°C, 6.8-7.8 kbar for sample 07-16 (Fig. 9a) and at 800-810°C, 6.0-7.0 kbar for sample 07-35 (Fig. 10a), i.e. within the sillimanite stability field and approximately at the rutile to ilmenite transition. This is consistent with: (i) the widespread occurrence of sillimanite in both samples, its microstructural occurrence in sample 07-16 (e.g. it replaces both garnet and plagioclase corona around kyanite; Fig. 4h-i) suggesting that it is a late phase; (ii) rutile rimmed by ilmenite in the matrix.

Peak-T and P conditions are firstly constrained by microstructural observations, i.e. the type of aluminosilicate included in the peritectic garnet rim, that is kyanite for sample 07-16 (Fig. 4b) and sillimanite for sample 07-35 (Fig. 5a). This microstructural evidence implies that garnet rim grew in the kyanite (sample 07-16) vs. sillimanite (sample 07-35) stability field, respectively. This implies that garnet rim grew at P > 10 kbar (sample 07-16) and at P < 10 kbar (sample 07-35), respectively. Notwithstanding the possible effects of partial modification of the X_{Ca} growth zoning by diffusion, further constraints on T_{min} and P_{min} may be provided by the minimum X_{Fe} of garnet core and by the X_{Ca} of garnet rim, before the outermost sharp drop in X_{Ca} (07-16: X_{Fe}= 0.74-0.75; X_{Ca}=0.04-0.05; 07-35: X_{Fe}= 0.74-0.75; X_{Ca}=0.04-0.05). These compositional parameters give T_{min}

and P_{min} conditions of 790-800°C, 9.6-10.8 kbar in the kyanite stability field for sample 07-16 (Fig. 9a) and of 800-810°C, 7.8-8.5 kbar in the sillimanite stability field for sample 07-35 (Fig. 10a). For sample 07-35, the estimated T_{min} conditions are further confirmed by the results of re-melting experimental studies (Ferrero *et al.*, in press), showing that the melting temperature of nanogranites included in garnet is ~800°C. The resulting retrograde P-T paths suggest a nearly isothermal decompression for both the samples.

The estimated T_{min} conditions are too close to the *solidus* and this is inconsistent with widespread evidence that large portion of garnet grew in the presence of melt. This discrepancy suggests that: (a) peak-T conditions were higher than those inferred by garnet X_{Fe} isopleths, due to diffusional homogenisation of X_{Fe}, and (b) the *solidus* is displaced up-T because some melt was extracted during the prograde evolution. In fact, at the estimated T_{min} conditions the amount of melt predicted by the pseudosections is very low for both the samples (< 5 vol%) (Fig. SM10 and SM12). To address the first issue, two alternative retrograde P-T paths (decompression with cooling) are proposed in Fig. 9a and 10a, starting in field A but at higher T. A decompression associated with cooling is also more consistent with the late growth of sillimanite at least in sample 07-16 (see the sillimanite isomodes reported in Fig. SM10). Considering that there is no clear evidence that biotite was eliminated during partial melting, the maximum peak-T (T_{max}) is constrained by the Bt-out curve, located at about 840°C and 850°C for samples 07-16 and 07-35, respectively. Therefore, if there is an undetected T difference between the two samples, it has to be within the T-interval constrained by field A, that is of about 50°C. The issue of melt loss is addressed in the next section.

As concerning the uncertainties in the estimate of peak-P conditions, the key point is that peak-pressures for samples 07-16 and 07-35 are constrained above and below the kyanite-sillimanite transition, respectively, i.e. above and below ca. 10 kbar, by unquestionable microstructural evidence (the type of aluminosilicate present as inclusion in the garnet rim). This difference in peak-P conditions is also consistent with that inferred by the X_{Ca} isopleths of garnet, thus suggesting that the original X_{Ca} values could have not been extensively reset.

Some considerations about the prograde-to-peak evolution

The P-T pseudosections (Fig. 9b and 10b) calculated for samples 07-16 and 07-35 using the bulk compositions obtained after the reintegration of 15 mol % (07-16b, Table 2) and 16 mol% (07-35b, Table 2) of melt, model the evolution of the rocks in the case they started melting at the water saturated *solidus* (see details in the Appendix). The topologies at the high-T side of the pseudosections of Fig. 9b-10b and of Fig. 9a-10a (supra-*solidus* domains) are very similar (e.g. White & Powell, 2002; Indares *et al.*, 2008; Groppo *et al.*, 2010), as well as the locations of compositional isopleths within field A. According to the melt-reintegrated pseudosections, at the estimated T_{min} and P_{min} conditions (sample 07-16: 790-800°C, 9.6-10.8 kbar; sample 07-35: 800-810°C, 7.8-8.5 kbar) the total amount of melt predicted by the pseudosections is 15-17 vol% and 19-20 vol%, respectively; these should be considered as minimum estimates, because the modelled peak-T are minimum-T. These amounts of melt are appreciably higher than the critical threshold of 7-10 vol% required for melt to be able to escape from its source (e.g. Rosenberg & Handy, 2005; Brown, 2007); therefore, the modelled peak assemblages for samples 07-16 and 07-35 are compatible with the production of a significant amount of melt and its partial extraction during the P-T evolution of the rocks.

Further constraints on the prograde evolution of sample 07-16 are firstly given by microstructural observations. Garnet rim locally includes corroded crystals of kyanite (Fig. 4b): garnet growing during kyanite consumption is consistent with a peritectic garnet growth during isobaric heating (path 1 of Fig. 8) and/or heating and decompression within field A (path 2 of Fig. 8). The qualitative trend of X_{Ca} zoning (if not the absolute values) helps in discriminate between these two possible trajectories. The distribution of X_{Ca} isopleths in field A of Fig. 8b (see also Fig. SM11), in fact, suggests that a trajectory like path 1 alone cannot account for the differences between the X_{Ca} in garnet mantle and the X_{Ca} in the garnet rim, therefore a path of type 2 is more likely. This means that the garnet mantle and rim grew at progressively lower P and higher T, at supra-*solidus* conditions. Although a precise estimate of both T and P is not possible due to the potential for X_{Fe} and X_{Ca} diffusional homogenization, the X_{Ca} isopleths of garnet mantle (X_{Ca}=0.055-0.060) point to a minimum-P of 10.5-12.5 kbar at T<800°C (Fig. 9b). Garnet core for sample 07-16 shows a X_{Ca} higher than the mantle and no microstructural evidence for growth during partial melting. The more simple solution is that garnet core grew in the lower-T stability field of garnet-biotite-kyanite-white mica-liquid (field B in Fig. 9b): in this field, however, the amount of produced melt was very low (< 2 vol%) (Fig. SM11). Therefore, the mantle development should coincide with the first significant appearance of melt following the white mica de-hydration melting reaction R1.

Similarly to sample 07-16, in sample 07-35 first order constraints for the prograde P-T trajectory are provided by microstructural features. The presence of sillimanite included in some garnet rims, in fact, implies that R1 should have been crossed in the sillimanite stability field, since this is the last Al-silicate producing reaction along the prograde P-T path (Fig. SM9). The main consequence of this microstructural evidence is that a prograde nearly isobaric heating path (path 1 of Fig. 8) is more likely than a decompression with heating path (path 2 of Fig. 8; see also the garnet isomodes showing that, in both cases, the modal amount of garnet increases from less than 1 vol% at the *solidus* to ca. 5 vol% at peak-T). A nearly isobaric heating path is also consistent with the slight decrease of X_{Ca} from the garnet core to the rim (Fig. 6b). The X_{Ca} isopleths of the peritectic garnet core (X_{Ca}=0.050) point to a minimum-P of 7.5 kbar at T <800°C (Fig. 10b and Fig. SM13), in agreement with the stability of kyanite during the prograde evolution of sample 07-35.

DISCUSSION

P-T evolution of the Barun Gneiss

Microstructural relationships, mineral chemical data and thermodynamic modelling allowed constraining the P-T evolution of two representative samples of the Barun Gneiss, collected from different structural levels. The resulting P-T paths show a clockwise shape characterized by a prograde heating ± decompression at T between 800°C and 850°C (i.e. within field A: Fig. 9 and 10) followed by decompression down to pressures at which melt completely crystallized. Despite these common features, the two P-T paths differ for the pressure conditions at peak-T predicted by the pseudosections: peak-P above the Ky-Sil transition (i.e. above ca. 10 kbar) for the structurally lower sample 07-16 vs. peak-P below the Ky-Sil transition for the structurally upper sample 07-35 (Fig. 12). Similarly, final melt crystallization is inferred to have occurred at about 7.5 kbar and 6.5 kbar for samples 07-16 and 07-35, respectively. The lower equilibration pressures inferred for the structurally upper sample define a “normal” (i.e. not inverted) metamorphic sequence in the lower portion of the HHC. Moreover, the P-T evolution predicted by the pseudosection modelling is

dominated either by decompression (sample 07-16: ΔP=-4 kbar, ΔT=30°C) or heating (sample 07-35: ΔP=-2 kbar; ΔT=70°C).

Overall, our data confirm the clockwise P-T path proposed for the Barun Gneiss by Pognante & Benna (1993) along the same geological transect, although their estimated peak P and T are significantly lower. This discrepancy is likely due to the fact that these authors constrained the P-T evolution of the Barun Gneiss using conventional thermobarometry, which could have given results biased by the use of diffusionally-modified mineral compositions. Our P-T path is also similar in shape to that proposed by Streule *et al.* (2010): the significantly lower P and T estimated by these authors is due to the appearance of cordierite replacing garnet in the structurally higher portion of the Barun Gneiss, as already described by Pognante & Benna (1993).

In contrast, our P-T paths differ greatly from the counterclockwise trajectory proposed by Goscombe & Hand (2000) for the same transect, although the P-T conditions they estimated for the matrix assemblage roughly coincide with our P-T conditions of melt crystallization (Fig. 12). The prograde portion of their trajectory was mainly based on two observations, namely: (i) the lack of kyanite in all the analysed samples, and (ii) the presence of rare spinel inclusions in garnet porphyroblasts. However, we have clearly shown that kyanite relicts are variably preserved in the Barun Gneiss (and also in the lateral equivalent Kangchenjunga Gneiss – Mosca *et al*., 2010), implying a decompressional or heating evolution from the kyanite to the sillimanite field. The presence of spinel limited to inclusions in garnet suggest that its growth may be due to high-T reactions occurring in very local SiO_2-undersaturated microdomains.

Was the partial melting in the Barun Gneiss triggered by heating or decompression?

The preservation of the granulitic peak assemblages in both the studied samples suggests that they experienced a significant melt loss during their metamorphic evolution (e.g. White & Powell, 2002; Brown, 2007). Although it is not possible to quantify the exact amount of melt segregated from the Barun Gneiss as a whole, this observation is consistent with the presence of abundant concordant and discordant granitic dykes crosscutting the Barun Gneiss. This consideration arises some questions about: (i) how much melt was likely produced by the Barun Gneiss and through which reactions, and (ii) whether partial melting in the Barun Gneiss was triggered by decompression (as often suggested for the Higher Himalayan Crystallines; e.g. Harris & Inger, 1992; Harris & Massey, 1994; Patiño Douce & Harris, 1998; Harris *et al*., 2004; Streule *et al*., 2010; Searle *et al*., 2010) or by heating.

The P-T pseudosections calculated for the melt-reintegrated compositions (07-16b and 07-35b, Table 2) represent end-member cases likely approximating the behaviour of the pelitic protoliths of the studied samples. According to our modelling, for this kind of source rocks, the main melt-producing reactions are reactions R1 and R2: the related melt productivity depends on (i) the slope of melt isomodes in the P-T space (which in turn is an expression of the slope of the reaction curve), and (ii) the angle at which the P-T trajectory crosses the melt isomodes.

Reaction R1 (muscovite de-hydration melting) represents the first main episode of melt production in the studied rocks: it has a moderately positive slope, therefore the amount of melt produced through this reaction is almost independent from the P-T path being an heating-dominated vs. a decompression-dominated trajectory. On the contrary, reaction R2 (biotite de-hydration melting) has a steep positive slope, therefore the amount of melt produced through this reaction strongly depends on how the P-T path crosses field A. In particular, significant amounts of melt (up to 20 vol%) can be produced during nearly isobaric heating or during decompression associated to

heating. On the contrary, during nearly isothermal decompression, melt may be produced only in very small amounts (less than 10 vol%). This is consistent with the results of several experimental studies on aluminous metasediments, which suggest that, although there is an observable effect of pressure on melt productivity, this effect is not strong (e.g. Patiño Douce & Johnston, 1991; Steven *et al*., 1997).

Despite the uncertainties in the reconstruction of the prograde evolution of the studied samples, our results qualitatively show that:

(i) sample 07-16 crossed both reactions R1 and R2 along an heating decompression path. The maximum amount of melt that would have been produced through reactions R1 and R2 (if no melt loss had occurred: Fig. SM11) was 13-15 vol% (R1) and 7-10 vol% (R2), respectively;

(ii) sample 07-35 crossed both reactions R1 and R2 along a nearly isobaric heating path. The maximum amount of melt that would have been produced through reactions R1 and R2 (if no melt loss had occurred: Fig. SM13) was 10-12 vol% (R1) and 8-12 vol% (R2), respectively.

It can therefore be suggested that, given the inferred P-T paths and their relations with the main melt-producing reactions in the P-T space, melt production in the Barun Gneiss was mainly triggered by heating, with or without the combined effect of decompression. Decompression alone is not able to explain the production of large amounts of melt. In particular, it can be concluded that a significant amount of melt was produced in the Barun Gneiss prior to decompression at depths of 25-35 km, in agreement with the conclusions of Streule *et al.* (2010).

It is worth noting that a similar conclusion (i.e. melt production was mainly triggered by heating) was already reached by Guilmette *et al*. (2011) for anatectic paragneisses from the Namche Barwa, eastern Himalayan Syntaxis, which experienced a P-T evolution similar to that inferred for the studied Barun Gneiss samples although at higher P-T conditions (ca. 850°C, 15 kbar). Comparisons with the P-T evolutions and melt productivities inferred by previous studies for other HT-HP anatectic paragneiss in the HHC of eastern Himalaya (e.g. Sikkim: Neogi *et al*., 1998; Dasgupta *et al*., 2004; Bhutan: Davidson *et al*., 1997; Daniel *et al*., 2003; Namche Barwa: Liu & Zhong, 1997) are complicated by the different approaches used to estimate: (i) peak P-T conditions, (ii) P-T trajectories, and (iii) the amount of melt produced during prograde evolution. Further detailed studies considering the possibility of melt loss during the prograde evolution of these HT-HP rocks are therefore needed to confirm if the P-T evolution and melt production history inferred for the Barun Gneiss may be applied to the whole HHC in eastern Himalaya.

Comparison between the Barun Gneiss P-T evolution and the "channel flow" model predictions

The "channel flow" tectonic model (Beaumont *et al.*, 2001, 2004; Jamieson *et al.*, 2004, 2006; Grujic *et al.*, 2006), has become one of the most popular paradigms to explain the tectonometamorphic evolution of the HHC and, more generally, the first-order features of the Himalayan-Tibetan orogen. According to such model, the HHC represents the surface expression of a low-viscosity middle crustal layer which may extend underneath the Tibetan plateau. Its present position would be related to the combined effect of lateral extrusion due to the overburden and focussed erosion, triggered by the monsoons, on the southern side of the Himalayas. The reliability of this thermal-mechanical model has been investigated by several authors using a multidisciplinary approach, involving geological, structural, petrological, geophysical and geochronological studies

(e.g. Godin *et al.*, 2006; Imayama *et al.*, 2010). Petrology has given an important contribution to the debate on the applicability of such model to the Himalayas, providing evidence both in favour (e.g. Grujic *et al*., 2002; Hollister & Grujic, 2006; Imayama *et al.*, 2010; Streule *et al*., 2010) and against it (e.g. Kohn, 2008).

As concerning the HHC, the most significant geologic and petrologic predictions of the "channel flow" model are (from Jamieson *et al.*, 2004):

(1) A clockwise P-T evolution, characterized by: (i) prograde burial and heating along relatively steep dP/dT prograde paths in the kyanite field; (ii) near-isothermal decompression, and (iii) final cooling and decompression along moderate dP/dT retrograde paths in the sillimanite (and more rarely andalusite-) field.

(2) The lower structural levels of the HHC (i.e. those rocks which are entrained within the hot channel, G1 in Fig. 12) record a nearly isothermal decompression, whereas the higher structural levels of the HHC (i.e. those rocks which flows outwards with the underlying channel, G2 in Fig. 12) record a near-isobaric heating. The modelled pressures at peak-T are 7-13 kbar (T_{max} = 720-820°C) in the first case and 4-6 kbar (T_{max} = 450-600°C) in the second case.

(3) Metamorphic peak pressure and temperature (P_{max} and T_{max}) conditions progressively decrease structurally upward in the HHC, thus defining a "normal" metamorphic sequence, interpreted as an exhumed crustal section. This is in contrast with the well known inverted metamorphic sequence that characterizes the lowermost MCTZ (e.g. Goscombe & Hand, 2001; Goscombe *et al*., 2006; Groppo *et al*., 2009).

(4) The distance between rocks which are entrained in the hot channel significantly decreases (i.e. from 70 to ca. 10 km), consistently with thrust-sense displacement, whereas the separation between rocks overlying the channel increases, consistently with normal-sense displacement.

(5) The maximum burial depth (P_{max}) was reached at 28-32 Ma, corresponding to the time at which the HHC material was entrained with the outward flowing channel, whereas the maximum temperature (T_{max}) was reached at ca. 16-20 Ma.

Our geologic and petrologic data and the resulting P-T paths for samples 07-16 and 07-35 are consistent with the expectations of the "channel flow" model, including:

(1) the overall clockwise shape of the P-T paths and: (i) the decompression-dominated P-T path of the structurally lower sample 07-16, reflecting the progressive exhumation of rocks that were entrained in the deep, high-T region of the channel, where they experienced gradually declining pressures at nearly constant or slightly decreasing temperature; (ii) the heating-dominated P-T path of the structurally upper sample 07-35, reflecting the evolution of those rocks which flowed outwards with the underlying channel (Fig. 12);

(2) the estimated pressures at peak-T, which are perfectly in agreement with those derived from the model (our data: P_{min}=10 to 8 kbar at 800°C; model G1: 13 to 7 kbar at 800°C) (Fig. 12);

(3) the decreasing pressure structurally upward, which defines a "normal" metamorphic sequence, in contrast to the inverted metamorphic sequence occurring in the lowermost MCTZ. Preliminary field and petrographic observations (Table SM1) suggest that pressures at T_{max} further decrease structurally upward, leading to the appearance of cordierite and andalusite (see also Pognante & Benna, 1993 and Streule *et al.*, 2010). However, our data suggest that T_{max} are quite uniform at different structural levels, in contradiction with the upward decreasing in T predicted by the "channel flow" model. This discrepancy may be ascribed to the advective heat transfer due to melt migration (not considered in the model), which can provide a large amount

of heat towards the structurally higher levels of the Barun Gneiss (e.g. Depinein *et al.*, 2008; Imayama *et al.*, 2010).

(4) The studied samples were collected from the lowermost structural levels of the HHC (Barun Gneiss, cf. geological setting): therefore, according to the "channel flow" model as defined by Beaumont *et al.* (2001) and Jamieson *et al.* (2004), our samples correspond to those rocks that were entrained within the channel and that were extruded immediately above the MCTZ. The actual lateral separation between the studied samples is about 10 km.

The petrologic constraints provided in this study are not conclusive evidence that the "channel flow" was the mechanism responsible for the structural architecture of the Himalayan chain, because they could be equally applicable to the predictions of other thermo-mechanical models (e.g. Grujic *et al*., 2002; Kohn, 2008); however, our results are certainly consistent with the predictions of the "channel flow" model and, although not sufficient to demonstrate its validity, they clearly do not exclude that the channel flow may have been the main process that really worked in the Himalayas. Geochronological data from the sampled location would be useful in order to further test the proposed consistency of our data with the predictions of the "channel flow" model.

CONCLUDING REMARKS

- The studied Grt-Kfs-Ky-Sil Barun Gneiss from the Arun-Barun transect (eastern Nepal) show several microstructural evidence of widespread de-hydration melting of biotite, including the peritectic growth of garnet and K-feldspar at the expenses of kyanite/sillimanite, biotite and plagioclase.
- The P-T evolution of the Barun Gneiss has been constrained using the thermodynamic approach of P-T pseudosections. Basing on the overall topologies of the pseudosections (P-T location of field A) and microstructural information (the type of aluminosilicate inclusion at garnet rims), it may be concluded that both the studied samples experienced a clockwise P-T evolution. However, a decompression-dominated vs. heating-dominated P-T path has been constrained for the structurally lower vs. upper sample, respectively. Peak-P conditions of the structurally lower sample are higher than those of the upper sample (for a similar peak-T of ca. 800°C), thus defining a "normal" metamorphic sequence.
- Melt production in the Barun Gneiss was likely related to both the white mica- and the biotite-de-hydration melting, and was mainly triggered by heating, with or without the combined effect of decompression. In other words, decompression alone is not able to explain the production of large amounts of melt, in contrast with what is often suggested for the Higher Himalayan Crystallines.
- The P-T evolution constrained for the Barun Gneiss is consistent with the predictions of the "channel flow" model, which is actually one of the most suitable paradigms to explain the tectonometamorphic evolution of the HHC in the Himalayan-Tibetan orogen.

ACKNOWLEDGEMENTS

We gratefully acknowledge S. Ferrero and B. Cesare for their help in the identification of nanogranites, for having shared their experimental data on re-melting and homogenization of nanogranites and for useful discussion on crustal anatexis, and B. Lombardo for the constructive discussion on Himalayan geology. R. Cossio and G. Vaggelli helped in acquiring μ-XRF maps with

the instrument acquired by the Interdepartmental Center "G. Scansetti". L. Martire helped in acquiring the CL images, with the equipment provided by the CNR IGG, Torino section. Constructive comments by D. Kelsey, C. Warren and an anonymous reviewer, that considerably improved the paper, were greatly appreciated, as well as the helpful suggestions, constructive criticisms and editorial handling by J. Hermann.

FUNDING

Fieldwork was carried out thanks to contributions from the Italian National Research Council (F.R.) and from PRIN Cofin 2006 (C.G.). Laboratory work was supported by PRIN Cofin 2006.

SUPPLEMENTARY DATA

Supplementary data for this paper are available at Journal of Petrology online.

APPENDIX

Mineral chemistry

The rock-forming minerals were analysed with a Cambridge Stereoscan 360 SEM equipped with an EDS Energy 200 and a Pentafet detector (Oxford Instruments) at the Department of Mineralogical and Petrological Sciences, University of Torino. The operating conditions were: 50 seconds counting time and 15 kV accelerating voltage. SEM-EDS quantitative data (spot size = 2μm) were acquired and processed using the Microanalysis Suite Issue 12, INCA Suite version 4.01; natural mineral standards were used to calibrate the raw data; the ΦρZ correction (Pouchou & Pichoir, 1988) was applied.

Cathodoluminescence images

Cathodoluminescence images have been acquired using a CITL 8200 mk3 equipment operating with 15-17 kV and a current of 400-500 mA, installed at the Dept. of Earth Sciences, University of Torino. In all the cathodoluminescence images: blue = K-feldspar; green = plagioclase; red = kyanite; dark red = sillimanite; very dark-blue = quartz; black = garnet or biotite.

Micro-XRF maps of the thin sections

Qualitative major elements X-ray maps of the whole thin sections have been acquired using a μ-XRF Eagle III-XPL spectrometer equipped with an EDS Si(Li) detector and with an Edax Vision32 microanalytical system, located at the Department of Mineralogical and Petrological Sciences, University of Torino (Italy). The operating conditions were: 100 msec counting time, 40 kV accelerating voltage and a probe current of 900 μA. A spatial resolution of about 65 μm in both x and y directions has been used. Quantitative modal amounts of each mineral phase have been obtained by processing the μ-XRF maps with the software program Petromod (Cossio *et al.*, 2002).

Estimate of the bulk compositions of the studied samples (07-16 and 07-35)

The bulk rock compositions of samples 07-16 and 07-35 (07-16a and 07-35a, Table 2) for the thermodynamic modelling have been calculated by combining the mineral proportions obtained from the modal estimate of the micro-XRF maps with mineral chemistry acquired at SEM-EDS. This method was preferred to the conventional methods such as ICP-MS or XRF because the precise estimate of the biotite modal percentage is required to derive the H_2O content in the bulk. H_2O was derived from the modal proportion of biotite and using the biotite Ti-H substitution scheme of White *et al.* (2007) (see Indares *et al.*, 2008 for further details). To avoid the possible biotite overestimation due to its preferred orientation, the thin sections have been obtained cutting the samples perpendicularly to the main foliation and lineation.

Melt-reintegrated compositions likely approximating the protolith compositions (07-16b and 07-35b, Table 2) have been calculated by re-integrating 15 mol% and 16 mol% of melt to the measured bulk compositions, respectively. These amounts of melt are those required to model a water saturated *solidus* in the P range of interest (the water saturated *solidus* is located at about 670°C and it is not reported in Fig. 9b and 10b). The composition of re-integrated melt has been calculated at 790°C, 11 kbar.

Pseudosection modelling of the Barun Gneisses (samples 07-16 and 07-35)

Samples 07-16 and 07-35 have been modelled in the system MnNCKFMASTH; Fe^{+3} was neglected because Fe^{+3}-rich oxides are lacking and the amount of Fe^{+3} in the analysed minerals is very low. Pseudosections have been calculated using Perplex (version 09 – Connolly 1990, 2009) and the internally consistent thermodynamic dataset and equation of state for H_2O of Holland & Powell (1998, revised 2004). The minerals considered in the calculation were: garnet, plagioclase, K-feldspar, quartz, biotite, white mica, cordierite, spinel, orthopyroxene, kyanite, sillimanite, andalusite, rutile and ilmenite. The following solid solution models were used: phengite and garnet (Holland & Powell, 1998), Ti-biotite (White *et al.*, 2007), plagioclase (Newton *et al.*, 1980), K-feldspar (Thompson & Hovis, 1979), orthopyroxene (Powell & Holland, 1999), cordierite (ideal model) and silicate-melt (Holland & Powell, 2001; White *et al.*, 2001). The fluid was considered as pure H_2O.

REFERENCES

Auzenneau, E., Vielzeuf, D. & Schmidt, M.W. (2006). Experimental evidence of decompression melting during exhumation of subducted continental crust. *Contribution to Mineralogy and Petrology* **152**, 125–148.

Barbey, P., Brouand, M., Le Fort, P. & Pecher A. (1996). Granite-migmatite genetic link: the example of the Manaslu granite and Tibetan Slab migmatites in central Nepal. *Lithos* **38**, 63–79.

Beaumont, C., Jamieson, R.A., Nguyen, M.H. & Lee, B. (2001). Himalayan tectonics explained by extrusion of a low-viscosity crustal channel coupled to focused surface denudation. *Nature* **414**, 738–742.

Beaumont, C., Jamieson, R.A., Nguyen, M.H. & Medvedev, S. (2004). Crustal channel flows: 1. Numerical models with applications to the tectonics of the Himalayan-Tibetan orogen. *Journal of Geophysical Research* **109**, B06406.

Bordet, P. (1961). *Recherches géologiques dans l'Himalaya du Népal, région du Makalu*. Editions du Centre National de la Recherche Scientifique, Paris, 275 p.

Brown, M. & Rushmer, T. (2006). *Evolution and differentiation of the continental crust*. Cambridge University Press, Cambridge, UK, 553 p.

Brown, M. (1994). The generation, segregation, ascent and emplacement of granite magma: the migmatite-to-crustally derived granite connection in thickened orogens. *Earth Science Reviews* **36**, 83–130.

Brown, M. (2002). Retrograde processes in migmatites and granulites revisited. *Journal of Metamorphic Geology* **20**, 24–40.

Brown, M. (2007). Crustal melting and melt extraction, ascent and emplacement in orogens: mechanism and consequences. *Journal of Geological Society of London* **164**, 709–730.

Brunel, M. & Kienast, J.R. (1986). Etude pétro-structurale des chevauchements ductiles himalayens sur la transversale de l'Everest-Makalu (Népal oriental). *Canadian Journal of Earth Sciences* **23**, 1117–1137.

Caddick, M.J., Konopásek, J. & Thompson, A.B. (2010). Preservation of garnet growth zoning and the duration of prograde metamorphism. *Journal of Petrology* **51**, 2327–2347.

Catlos, E.J., Dubey, C.S., Harrison, T.M. & Edwards, M.A. (2004). Late Miocene movement within the Himalayan Main Central Thrust shear zone, Sikkim, north-east India. *Journal of Metamorphic Geology* **22**, 207–226.

Cenki, B., Kriegsman, L.M. & Braun, I. (2002). Melt-producing and melt-consuming reactions in the Achankovil cordierite gneisses, South India. *Journal of Metamorphic Geology* **20**, 543–561.

Cesare, B., Ferrero, S., Salvioli-Mariani, E., Pedron, D. & Cavallo, A. (2009). "Nanogranite" and glassy inclusions: the anatectic melt in migmatites and granulites. *Geology* **37**, 627–630.

Clemens, J.D. & Vielzeuf, D. (1987). Constraints on melting and magma production in the crust. *Earth and Planetary Science Letters* **86**, 287–306.

Clemens, J.D. (1990). The granulite-granite connexion. In: Vielzeuf, D., & Vidal, P. (eds.) *Granulites and crustal differentiation*. Dordrecht, Kluwer Academic Publishers, 25–36.

Clemens, J.D. (2006). Melting of the continental crust: Fluid regimes, melting reactions, and source-rock fertility. In: Brown, M. & Rushmer, T. (eds.) *Evolution and differentiation of the continental crust*. Cambridge University Press, Cambridge, UK, 296–331.

Coggon, R. & Holland, T.J.B. (2002). Mixing properties of phengitic micas and revised garnet–phengite thermobarometers. *Journal of Metamorphic Geology* **20**, 683–696.

Connolly, J.A.D. & Kerrick, D.M. (1987). An algorithm and computer program for calculating composition phase diagrams. *CALPHAD* **11**, 1–55.

Connolly, J.A.D. (1990). Multivariable phase diagrams: an algorithm based on generalize thermodynamics. *American Journal of Science* **290**, 666–718.

Connolly, J.A.D. (2009). The geodynamic equation of state: what and how. *Geochemistry, Geophysics, Geosystems* **10**, Q10014.

Cossio, R., Borghi, A. & Ruffini, R. (2002). Quantitative modal determination of geological samples based on X-ray multielemental map acquisition. *Microscopy and Microanalysis* **8**, 139–149.

Daniel, C.G., Hollister, L.S., Parrish, R.R. & Grujic, D. (2003). Exhumation of the Main Central Thrust from lower crustal depths, Eastern Bhutan Himalaya. *Journal of Metamorphic Geology* **21**, 317–334.

Dasgupta, S., Ganguly, J. & Neogi, S. (2004). Inverted metamorphic sequence in the Sikkim Himalayas: crystallization history, P–T gradient and implications. *Journal of Metamorphic Geology* **22**, 395–412.

Davidson, C., Grujic, D.E., Hollister, L.S. & Schmid, S.M. (1997). Metamorphic reactions related to decompression and synkinematic intrusion of leucogranite, High Himalayan Crystallines, Bhutan. *Journal of Metamorphic Geology* **15**, 593–612.

Depinein, V.G., Andronicos, C.L. & Morgan, J.P. (2008). Near-isothermal conditions in the middle and lower crust induced by melt migration. *Nature* **452**, 80–83.

Ferrero, S., Bartoli, O., Cesare, B., Salvioli Mariani, E., Cavallo, A., Groppo, C. & Battiston, S. (in press). Microstructures of melt inclusions in anatectic metasedimentary rocks. *Journal of Metamorphic Geology* (in press).

Florence, F.P. & Spear, F.S. (1991). Effects of diffusional modification of garnet growth zoning on P-T path calculations. *Contributions to Mineralogy and Petrology* **107**, 487–500.

Fyfe, W.S. (1973). The granulite facies, partial melting and the Archean crust. *Philosophical Transactions of the Royal Society of London* **273**, 457–461.

Gardien, V., Thompson, A.B., Grujic, D. & Ulmer, P. (1995). Experimental melting of biotite + plagioclase + quartz ± muscovite assemblages and implications for crustal melting. *Journal of Geophysical Research* **100**, 15581–15591.

Godin, L., Grujic, D., Law, R. & Searle, M.P. (2006). Crustal flow, extrusion, and exhumation in continental collision zones: an introduction. In: Law, R., Searle, M.P. & Godin, L. (eds.) *Channel flow, ductile extrusion, and exhumation in continental collision zones*. Geological Society of London, Special Publication **268**, London, 1–23.

Godin, L., Grujic, D., Law, R.D. & Searle, M.P. (2006). Channel flow, ductile extrusion and exhumation in continental collision zones: an introduction. In: Law, R.D., Searle, M.P. & Godin, L. (eds.) *Channel Flow, Ductile Extrusion and Exhumation in Continental Collision Zones*. Geological Society of London, Special Publications **268**, London, 1–23.

Godin, L., Parrish, R.R., Brown, R.L. & Hodges, K.V. (2001). Crustal thickening leading to exhumation of the Himalayan metamorphic core of central Nepal: Insights from U–Pb geochronology and $^{40}Ar/^{39}Ar$ thermochronology. *Tectonics* **20**, 729–747.

Goscombe, B. & Hand, M. (2000). Contrasting P-T paths in the Eastern Himalaya, Nepal: inverted isograds in a paired metamorphic mountain belt. *Journal of Petrology* **41**, 1673–1719.

Goscombe, B., Gray, D. & Hand, M. (2006). Crustal architecture of the Himalayan metamorphic front in eastern Nepal. *Gondwana Research* **10**, 232–255.

Groppo, C. & Rolfo, F. (2010). The P-T evolution of the Barun Gneiss (Higher Himalayan Crystallines of Eastern Nepal) in the framework of the "channel flow" model. *Journal of Nepal Geological Society* (Special Issue) **41**, 8.

Groppo, C., Rolfo, F. & Lombardo, B. (2009). P-T evolution across the Main Central Thrust Zone (Eastern Nepal): hidden discontinuities revealed by petrology. *Journal of Petrology* **50**, 1149–1180.

Groppo, C., Rubatto, D., Rolfo, F. & Lombardo, B. (2010). Early Oligocene partial melting in the Main Central Thrust Zone (Arun Valley, eastern Nepal Himalaya). *Lithos* **118**, 287–301.

Grujic, D., Coutand, E., Bookhagen, B., Bonnet, S., Blythe, A. & Duncan, C. (2006). Climatic forcing of erosion, landscape, and tectonics in the Bhutan Himalayas. *Geology* **34**, 801–804.

Grujic, D., Hollister, L.S. & Parrish, R.R. (2002). Himalayan metamorphic sequence as an orogenic channel: insight from Bhutan. *Earth and Planetary Science Letters* **198**, 177–191.

Guernina, S. & Sawyer, E.W. (2003). Large-scale melt-depletion in granulite terranes: an example from the Archean Ashuanipi Subprovince of Quebec. *Journal of Metamorphic Geology* **21**, 181–201.

Guilmette, C., Indares, A. & Hébert, R. (2010). High-pressure anatectic metapelites from the Namche Barwa, Eastern Himalayan Syntaxis: textural evidence for partial melting, phase equilibria modelling and tectonic implications. *Lithos* **124**, 66-81.

Guiraud, M., Powell, R. & Rebay, G. (2001). H_2O in metamorphism and unexpected behaviour in the preservation of metamorphic mineral assemblages. *Journal of Metamorphic Geology* **19**, 445–454.

Harris, N.B.W., Caddick, M., Kosler, J., Goswami, S., Vance, D. & Tindle, A.G. (2004). The pressure–temperature–time path of migmatites from Sikkim Himalaya. *Journal of Metamorphic Geology* **22**, 249–264.

Harrison, T.M., Grove, M., McKeegan, K.D., Coath, C.D., Lovera, O.M. & LeFort, P. (1999). Origin and episodic emplacement of the Manaslu Intrusive Complex, Central Himalaya. *Journal of Petrology* **40**, 3–19.

Herron, M.M. (1988). Geochemical classification of terrigenous sands and shales from core or log data. *Journal of Sedimentary Petrology* **58**, 820–829.

Hodges, K.V., Parrish, R.R., Housh, T.B., Lux, D.R., Burchfiel, B.C., Royden, L.H. & Chen, Z. (1992). Simultaneous Miocene extension and shortening in the Himalayan orogen. *Science* **258**, 1466–1469.

Holland, T.J.B. & Powell, R. (1998). An internally consistent thermodynamic data set for phases of petrologic interest. *Journal of Metamorphic Geology* **16**, 309–343.

Holland, T.J.B.& Powell, R. (2001). Calculation of phase relations involving haplogranitic melts using an internally consistent thermodynamic dataset. *Journal of Petrology* **42**, 673–683.

Hollis, J.A., Harley, S.L., White, R.W. & Clarke, G.L. (2006). Preservation of evidence for prograde metamorphism in ultrahigh-temperature, high-pressure kyanite-bearing granulites, South Harris, Scotland. *Journal of Metamorphic Geology* **24**, 263–279.

Hollister, L.S. & Grujic, D. (2006). Pulsed channel flow in Bhutan. In: Law, R.D., Searle, M.P. & Godin, L. (eds) *Channel Flow, Extrusion, and Exhumation in Continental Collision Zones*. Geological Society of London, Special Publications **268**, London, 415–423.

Holness, M.B. & Clemens, J.D. (1999). Partial melting of the Appin Quartzite driven by fracture controlled H_2O infiltration in the aureole of the Ballachulish Igneous Complex, Scottish Highlands. *Contributions to Mineralogy and Petrology* **136**, 154–168.

Holness, M.B. & Sawyer, E.W. (2008). On the pseudomorphing of melt-filled pores during the crystallization of migmatites. *Journal of Petrology* **49**, 1343–1363.

Imayama, T., Takeshite T. & Arita K. (2010). Metamorphic P-T profile and P-T path discontinuity across the far-eastern Nepal Himalaya: investigation of channel flow models. Journal *of Metamorphic Geology* **28**, 527–549.

Indares, A., White, R.W. & Powell, R. (2008). Phase equilibria modelling of kyanite-bearing anatectic paragneiss from the central Grenville Province. *Journal of Metamorphic Geology* **26**, 815–836.

Jamieson, R.A., Beaumont, C., Medvedev, S. & Nguyen, M.H. (2004). Crustal channel flows: 2. Numerical models with implications for metamorphism in the Himalayan–Tibetan orogen. *Journal of Geophysical Research* **109**, B06407.

Jamieson, R.A., Beaumont, C., Nguyen, M.H. & Grujic, D. (2006). Provenance of the Greater Himalayan Sequence and associated rocks: Predictions of channel flow models. In: Law, R., Searle, M.P. & Godin, L. (eds.) *Channel flow, ductile extrusion, and exhumation in continental collision zones*. Geological Society of London, Special Publication **268**, London, 165–182.

Janàk, M., Hurai, V., Ludhova, L., O'Brien, P.J. & Horn, E.E. (1999). Dehydration melting and devolatilization during exhumation of high-grade metapelites: the Tatra Mountains, western Carpathians. *Journal of Metamorphic Geology* **17**, 379–395.

Jessup, M.J., Cottle, J.M., Searle, M.P., Law, R.D., Newell, D.L., Tracy, R.J. & Waters, D.J. (2008). P–T–t–D paths of Everest Series schist, Nepal. *Journal of Metamorphic Geology* **26**, 717–739.

Johnson, T.E., White, R.W. & Powell, R. (2008). Partial melting of metagreywacke: a calculated mineral equilibria study. *Journal of Metamorphic Geology* **26**, 837–853.

Kellett, D.A., Grujic, D., Warren, C., Cottle, J., Jamieson, R. & Tenzin, T. (2010). Metamorphic history of a syn-convergent orogen-parallel detachment: The South Tibetan detachment system, eastern Himalaya. *Journal of Metamorphic Geology* **28**, 785-808.

Kohn, M.J. (2008). P–T–t data from central Nepal support critical taper and repudiate large-scale channel flow of the Greater Himalayan sequence. *Geological Society of America Bulletin* **120**, 259–273.

Kohn, M.J., Spear, F.S. & Valley, J.W. (1997). Dehydration melting and fluid recycling during metamorphism: Rangeley Formation, New Hampshire, USA. *Journal of Petrology* **38**, 1255–1277.

Kriegsman, L.M. & Álvarez-Valero, A.M. (2010). Melt-producing versus melt-consuming reactions in pelitic xenoliths and migmatites. *Lithos* 116, 310–320.

Le Breton, N. & Thompson, A.B. (1988): Fluid-absent (dehydration) melting of biotite in metapelites in the early stages of crustal anatexis. *Contributions to Mineralogy and Petrology* **99**, 226–237.

Liu, Y. & Zhong, D. (1997). Petrology of high-pressure granulitesfrom the eastern Himalayan syntaxis. *Journal of Metamorphic Geology* **15**, 451–466.

Lombardo, B., Pertusati, P. & Borghi, A. (1993). Geology and tectono-magmatic evolution of the eastern Himalaya along the Chomolungma-Makalu transect. In: Treloar, P.J. & Searle, M.P. (eds.) *Himalayan Tectonics*. Geological Society of London, Special Publication **74**, London, 341–355.

Marmo, B.A., Clarke, G.L. & Powell, R. (2002). Fractionation of bulk composition due to porphyroblast growth: effects on eclogite facies mineral equilibria, Pam Peninsula, New Caledonia. *Journal of Metamorphic Geology* **20**, 151–165.

Mohan, A., Windley, B.F. & Searle, M.P. (1989). Geothermobarometry and the development of inverted metamorphism in the Darjeeling-Sikkim region of the eastern Himalaya. *Journal of Metamorphic Geology* **7**, 95–110.

Montel, J.M. & Vielzeuf, D. (1997). Partial melting of metagreywackes, Part II. Compositions of minerals and melts. *Contribution to Mineralogy and Petrology* 128, **176**–196.

Mosca, P., Groppo, C. & Rolfo, F. (2010). New data on the geological setting of the Nepalese Kangchenjunga area. *Journal of Nepal Geological Society* (Special Issue) **41**, 17.

Neogi, S., Dasgupta, S. & Fukuoka, M. (1998). High-P–T polymetamorphism, dehydration melting, and generation of migmatites and granites in the Higher Himalayan Crystalline Complex, Sikkim, India. *Journal of Petrology* **39**, 61–99.

Newton, R.C., Charlu, T.V. & Kleppa, O.J. (1980). Thermochemistry of the high structural state plagioclases. *Geochimica et Cosmochimica Acta* **44**, 933–941.

O'Brien, P.J. (1997). Garnet zoning and reaction textures in overprinted eclogites, Bohemian Massif, European Variscides: A record of their thermal history during exhumation. *Lithos* **41**, 119–133.

O'Brien, P.J., Kröner. A., Jaeckel. P., Hegner, E., Żelaźniewicz, A. & Kryza, R. (1997). Petrological and Isotopic Studies on Palaeozoic High-pressure Granulites, Góry Sowie Mts, Polish Sudetes. *Journal of Petrology* **38**, 433–456.

Patiño Douce, A.E. & Beard, J.S. (1996). Effects of P, $f(O_2)$ and Mg/Fe Ratio on dehydration melting of model metagreywackes. *Journal of Petrology* **37**, 999–1024.

Patiño Douce, A.E. & Johnston, A.D. (1991). Phase equilibria and melt productivity in the pelitic system: implications for the origin of perallumionus granitoids and aluminous granulites. *Contributions to Mineralogy and Petrology* **107**, 202–218.

Patiño Douce, A.E. & Harris, N. (1998). Experimental constraints on Himalayan anatexis. *Journal of Petrology* **39**, 689–710.

Pattison, D.R.M., Chacko, T., Farquhar, J. & McFarlane, C.R.M. (2003). Temperatures of granulite-facies metamorphism: constraints from experimental phase equilibria and thermobarometry corrected for retrograde exchange. *Journal of Petrology* **44**, 867–900.

Pognante, U. & Benna, P. (1993). Metamorphic zonation, migmatization, and leucogranites along the Everest transect (Eastern Nepal and Tibet): record of an exhumation history. In: Treloar, P.J. & Searle, M.P. (eds.) *Himalayan Tectonics*. Geological Society of London, Special Publication **74**, London, 323–340.

Pouchou, J.L. & Pichoir, F. (1988). Determination of mass absorption coefficients for soft X-Rays by use of the electron microprobe. *Microbeam Analysis*, San Francisco Press, 319–324.

Powell, R. & Downes, J. (1990). Garnet porphyroblast-bearing leucosomes in metapelites: mechanisms, phase diagrams, and an example from Broken Hill, Australia. In: Ashworth, J.R. & Brown, M. (eds.) *High-Temperature Metamorphism and Crustal Anatexis*. The Mineralogical Society Series 2, Unwin-Hyman, London, 105–123.

Powell, R. & Holland, T. (1999). Relating formulations of the thermodynamics of mineral solid solutions: Activity modeling of pyroxenes, amphiboles, and micas. *American Mineralogist* **84**, 1–14.

Powell, R., Guiraud, M. & White, R.W. (2005). Truth and beauty in metamorphic phase equilibria: conjugate variables and phase diagrams. *Canadian Mineralogist* **43**, 21–33.

Rosenberg, C.L. & Handy, M.R. (2005). Experimental deformation of partially melted granite revisited: implications for the continental crust. *Journal of Metamorphic Geology* **23**, 19–28.

Sawyer, E.W. (1987). The role of partial melting and fractional crystallization determining discordant migmatite leucosome compositions. *Journal of Petrology* **28**, 445–473.

Sawyer, E.W. (1998). Formation and evolution of granite magmas during crustal reworking: the significance of diatexites. *Journal of Petrology* **39**, 1147–1167.

Sawyer, E.W., Dombrowski, C. & Collins, W.J. (1999). Movement of melt during synchronous regional deformation and granulite-facies anatexis, an example from the Wuluma Hills, central Australia. In: Castro, A., Fernandez, C. & Vigneresse, J.L. (eds.) *Understanding Granites: Integrating New and Classical Techniques.* Geological Society of London, Special Publication **168**, London, 221–237.

Searle, M.P. (1999). Extensional and compressional faults in the Everest-Lhotse massif, Khumbu Himalaya, Nepal. *Journal of the Geological Society of London* **156**, 227–240.

Searle, M.P., Law, R.D., Godin, L., Larson, K.P., Streule, M.J., Cottle, J.M. & Jessup, M.J. (2008). Defining the Himalayan Main Central Thrust in Nepal. *Journal of the Geological Society of London* **165**, 523–534.

Searle, M.P., Cottle, J.M., Streule, M.J. & Waters D.J. (2010). Crustal melt granites and migmatites along the Himalaya: melt source, segregation, transport and granite emplacement mechanisms. *Earth and Environmental Science Transactions of the Royal Society of Edinburgh* **100**, 219–233.

Spear, F.S. & Florence, F.P. (1992). Thermobarometry in granulites: Pitfalls and new approaches. *Journal of Precambrian Research* **55**, 209–241.

Spear, F.S. (1991). On the interpretation of peak metamorphic temperatures in light of garnet diffusion during cooling. *Journal of Metamorphic Geology* **9**, 379–388.

Spear, F.S., Kohn, M.J. & Cheney, J.T. (1999). P-T paths from anatectic pelites. *Contributions to Mineralogy and Petrology* **134**, 17–32.

Spear, F.S., Kohn, M.J., Florence, F. & Menard, T. (1990). A model for garnet and plagioclase growth in pelitic schists: Implications for thermobarometry and P-T path determinations. *Journal of Metamorphic Geology* **8**, 683–696.

Steven, G., Clemens, J.D. & Droop, G.D.R. (1997). Melt production during granulite-facies anatexis: experimental data from "primitive" metasedimentary protoliths. *Contributions to Mineralogy and Petrology* **128**, 352–370.

Štípská, P. & Powell, R. (2005). Constraining the P–T path of a MORB-type eclogite using pseudosections, garnet zoning and garnet-clinopyroxene thermometry: an example from the Bohemian Massif. *Journal of Metamorphic Geology* **23**, 725–743.

Štipská, P., Powell, R., White, R.W. & Baldwin, J.A. (2010). Using calculated chemical potential relationships to account for coronas around kyanite: an example from the Bohemian Massif. *Journal of Metamorphic Geology* **28**, 97–116.

Streule, M.J., Searle, M.P., Waters, D.J. & Horstwood, M.S.A. (2010). Metamorphism, melting and channel flow in the Greater Himalaya Sequence and Makalu leucogranite: constraints from thermobarometry, metamorphic modelling and U-Pb geochronology. *Tectonics* **29**, TC5011.

Swapp, S.M. & Hollister, L.S. (1991). Inverted metamorphism within the Tibetan slab of Bhutan: evidence for a tectonically transported heat-source. *Canadian Mineralogist* **29**, 1019–1041.

Tajčmanová, L., Konopásek, J. & Connolly, J.A.D. (2007). Diffusion-controlled development of silica undersaturated domains in felsic granulites of the Bohemian Massif (Variscan belt of Central Europe). *Contributions to Mineralogy and Petrology* **153**, 237–250.

Thompson, A.B. & Connolly, J.A.D. (1995). Melting of the continental-crust: some thermal and petrological constraints on anatexis in continental collision zones and other tectonic settings. *Journal of Geophysical Research* **100**, 15565–15579.

Thompson, A.B. (1982). Dehydration melting of pelitic rocks and the generation of H_2O-undersaturated granitic liquids. *American Journal of Science* **282**, 1567–1595.

Thompson, A.B. (2001). Clockwise P–T paths for crustal melting and H_2O recycling in granite source regions and migmatite terrains. *Lithos* **56**, 33–45.

Thompson, J.B. & Hovis, G.L. (1979). Entropy of Mixing in Sanidine. *American Mineralogist* **64**, 57–65.

Tinkham, D.K. & Ghent, E.D. (2005). Estimating P–T conditions of garnet growth with isochemical phase-diagram sections and the problem of effective bulk-composition. *The Canadian Mineralogist* **43**, 35–50.

Vanderhaeghe, O. (2001). Melt segregation, pervasive melt migration and magma mobility in the continental crust: The structural record from pores to orogens. *Physics and Chemistry of the Earth, Part A: Solid Earth and Geodesy* **26**, 213–223.

Vernon, R.H. & Collins, W.J. (1988). Igneous microstructures in migmatites. *Geology* **16**, 1126–1129.

Vielzeuf, D. & Holloway, J.R. (1988). Experimental determination of the fluid-absent melting relations in the pelitic system. *Contributions to Mineralogy and Petrology* **98**, 257–276.

Vielzeuf, D. & Montel, J.M. (1994). Partial melting of metagreywacke. Part I: fluid absent experiments and phase relationships. *Contributions to Mineralogy and Petrology* **117**, 375–393.

Vielzeuf, D. & Schmidt, M. (2001). Melting relations in hydrous systems revisited: application to metapelites, metagreywackes and metabasalts. *Contributions to Mineralogy and Petrology* **141**, 251–267.

Vielzeuf, D. & Vidal, P. (1990). *Granulites and crustal evolution*. Dordrecht, Kluwer Academic Publishers, The Netherlands, 585 p.

Vielzeuf, D., Clemens, J.C., Pin, C. & Moinet, E. (1990). Granites, granulites and crustal differentiation. In: Vielzeuf, D. & Vidal, P. (eds.) *Granulites and crustal differentiation.* Dordrecht, Kluwer Academic Publishers, The Netherlands, 59–85.

Visonà, D. & Lombardo, B. (2002). Two mica- and tormaline leucogranites from the Everest-Makalu region (Nepal-Tibet): Himalayan leucogranite genesis by isobaric heating? *Lithos* **62**, 125–150.

Waters, D.J. (2001). The significance of prograde and retrograde quartz-bearing intergrowth microstructures in partially melted granulite-facies rocks. *Lithos* **56**, 97–110.

White, R.W. & Powell, R. (2002). Melt loss and the preservation of granulite facies mineral assemblages. *Journal of Metamorphic Geology* **20**, 621–632.

White, R.W., Powell, R. & Halpin, A. (2004). Spatially-focussed melt formation in aluminous metapelites from Broken Hill, Australia. *Journal of Metamorphic Geology* **22**, 825–845.

White, R.W., Powell, R. & Holland, T.J.B. (2001). Calculation of partial melting equilibria in the system Na_2O-CaO-K_2O-FeO-MgO-Al_2O_3-SiO_2-H_2O (NCKFMASH). *Journal of Metamorphic Geology* **19**, 139–153.

White, R.W., Powell, R. & Holland, T.J.B. (2007). Progress relating to calculation of partial melting equilibria for metapelites. *Journal of Metamorphic Geology* **25**, 511–527.

Whitney, D.L., Teyssier, C. & Fayon, A.K. (2004). Isothermal decompression, partial melting and exhumation of deep continental crust. In: Grocott, J., Mc Caffrey, K.J.W., Taylor, G. & Tikoff, B. (eds.) *Vertical coupling and decoupling in the lithosphere*. Geological Society of London, Special Publication, **227**, London, 313–326.

Wolf, M.B. & London, D. (1994). Apatite dissolution into peraluminous haplogranitic melts: an experimental study of solubilities and mechanisms. *Geochimica and Cosmochimica Acta* **58**, 4127–4146.

Yardley, B.W.D. & Valley, J.W. (1997). The petrologic case for a dry lower crust. *Journal of Geophysical Research* **102**(B6), 12173–12185.

Zeitler, P.K., Meltzer, A.S., Koons, P.O., Craw, D., Hallet, B., Chamberlain, C.P., Kidd, W.S.F., Park, S.K., Seeber, L., Bishop, M. & Shroder J. (2001). Erosion, Himalayan geodynamics, and the geomorphology of metamorphism. *GSA Today* **11**, 4–8.

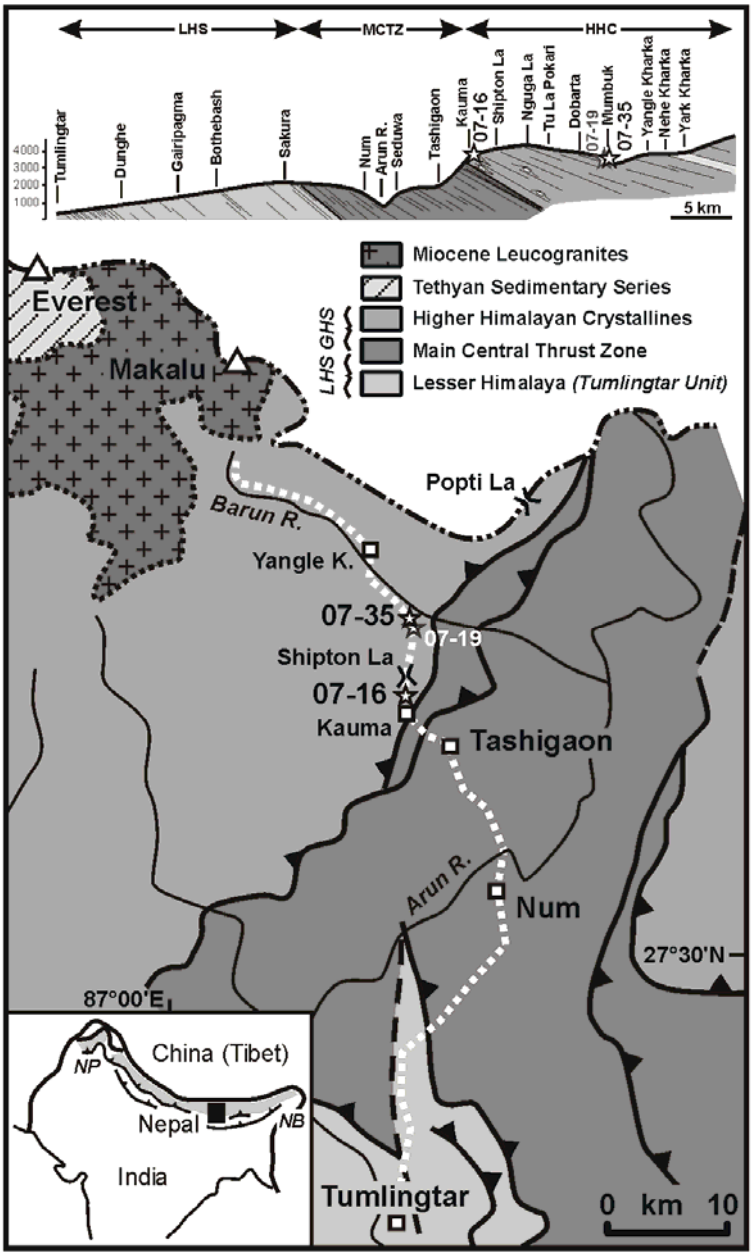

Fig. 1 – Geological sketch map of eastern Nepal from Everest to Tumlingtar across the middle Arun drainage and the Arun Tectonic Window, modified after Bordet (1961), Pognante & Benna (1993), Goscombe & Hand (2000) and Groppo *et al.* (2010). The north limit of the map (double dashed line) is the approximate political boundary between Nepal to the south, and China (Tibet) to the north. The Lesser Himalayan Sequence (LHS) and the Greater Himalayan Sequence (GHS) are sensu Goscombe *et al.* (2006). The highly idealised cross-section on top of the figure follows the path from Tumlingtar to the Makalu base camp (white dashed line on the map). Linear patterns in the cross section mimic the local attitude of regional foliation. Both the geologic sketch map and the cross section show the location of the studied samples (white stars). Inset shows the location of the study area (black rectangle) in the framework of the Himalayan chain. The grey shaded belt approximates the location of the Higher Himalayan Crystallines. NP: Nanga Parbat; NB: Namche Barwa.

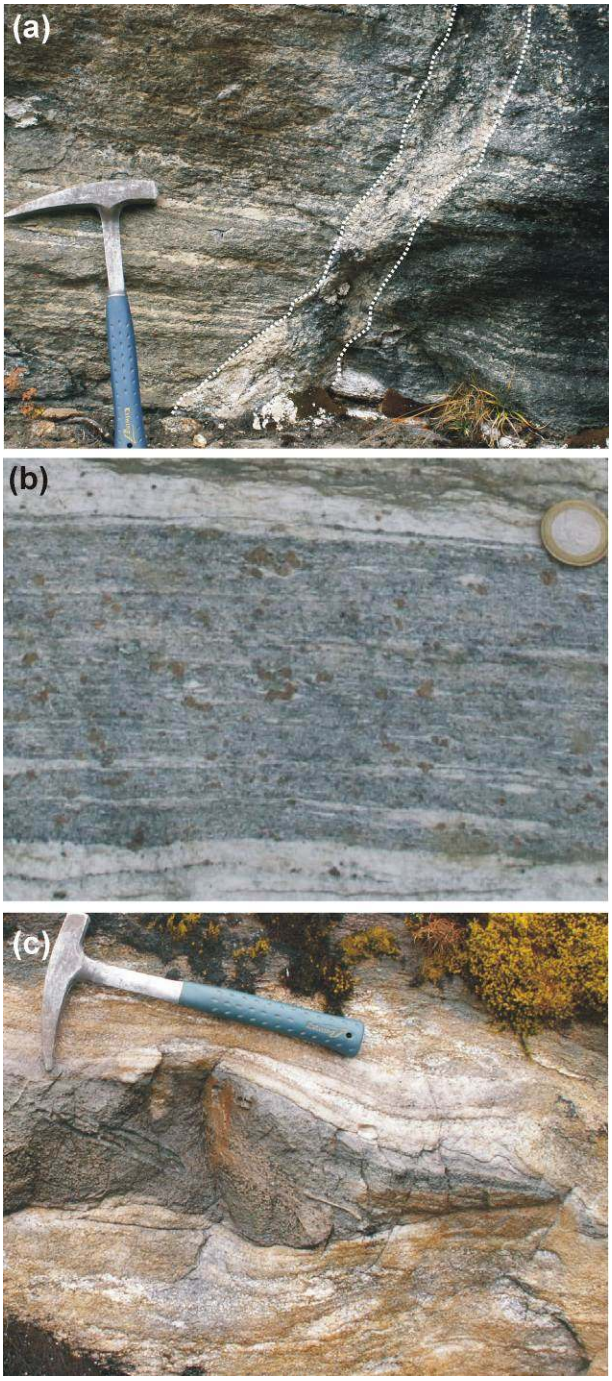

Fig.2 – Field pictures showing the main features of the Barun Gneiss at the outcrop scale. (a) The main foliation is defined by centimetric leucocratic quartzo-feldspathic domains alternating with dark biotite + plagioclase + sillimanite layers and is crosscut by a discordant decimetre-thick granitic dyke. (b) Detail of a dark biotite + plagioclase + sillimanite + garnet layer. (c) Boudin of calc-silicate granofels included in the Barun Gneisses and enveloped by the main foliation.

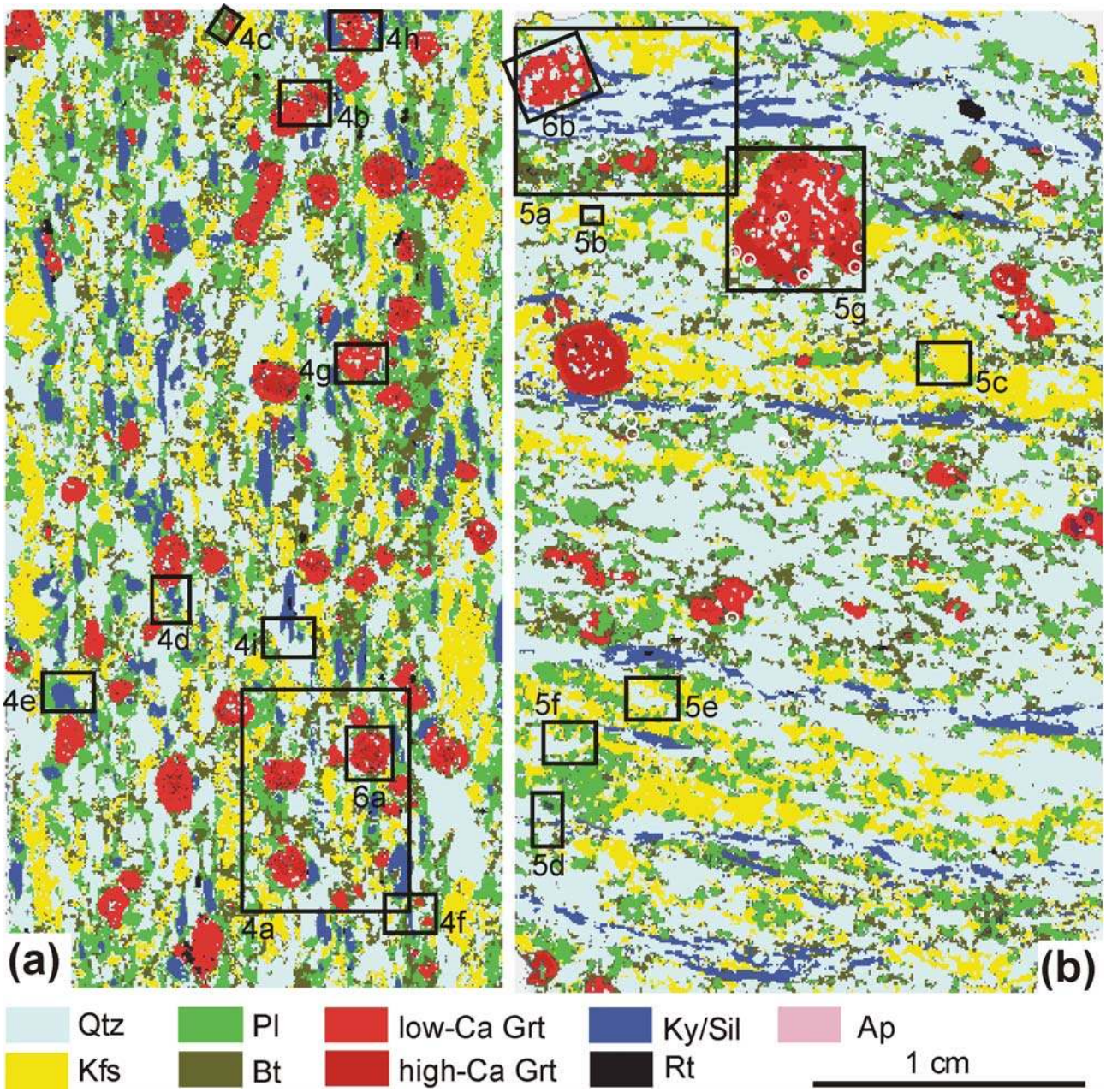

Fig. 3 – Major elements μ-XRF maps of the whole thin sections of the studied samples 07-16 (a) and 07-35 (b). Black boxes correspond to the microphotos of Fig. 4 and 5, respectively. White circles in (b) refer to apatite inclusions in garnet. Refer to the Appendix for the analytical technique.

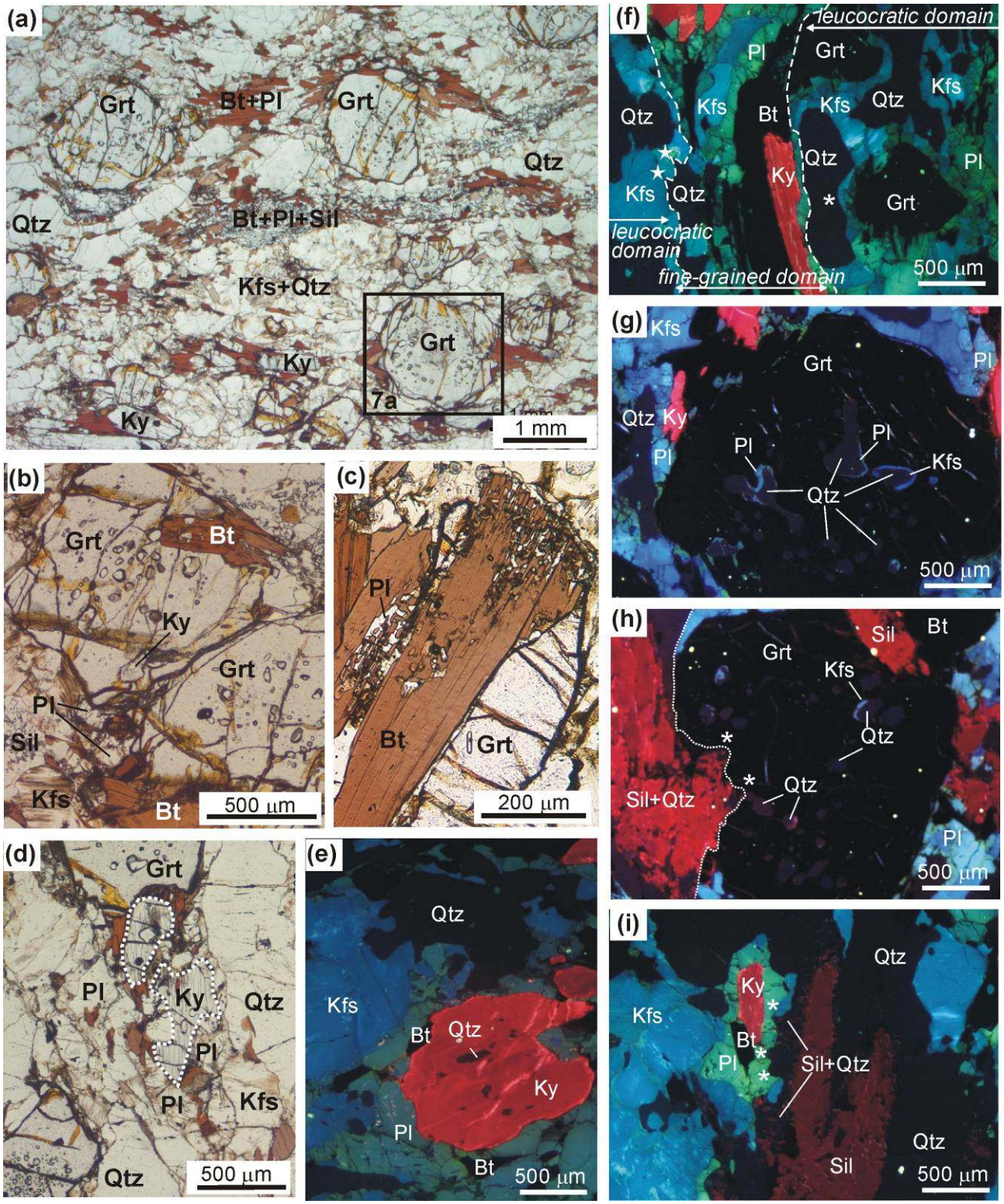

Fig. 4 – Representative microstructures of sample 07-16. **(a)** Garnet and kyanite porphyroblasts enveloped by the main foliation defined by dark fine-grained layers consisting of biotite + plagioclase + sillimanite alternated to coarse-grained domains mainly consisting of quartz + K-feldspar. Plane Polarized Light (PPL). **(b)** Detail of a garnet porphyroblast with a kyanite inclusion in the rim (PPL). **(c)** Detail of a biotite + plagioclase symplectite developed at the rim of porphyroblastic garnet (PPL). **(d)** Detail of a kyanite crystal partially corroded and surrounded by a biotite + plagioclase aggregate (PPL). **(e)** Zoned kyanite crystal partially corroded and surrounded by a plagioclase + biotite aggregate. Cathodoluminescence (CL) image (refer to the Appendix for the technique). **(f)** CL image showing coarse-grained quartzofeldspathic domains

alternating with a biotite + plagioclase + quartz layer. In the coarse-grained domain, a quartz ribbon is partially corroded by K-feldspar (asterisk). Conversely, quartz occurring in the biotite + plagioclase domain is fine-grained and partially replaces K-feldspar (stars). Note that kyanite is not in contact with quartz, but it is rimmed by plagioclase + biotite. **(g)** Detail of quartz inclusions in garnet mantle, surrounded by thin films of plagioclase and K-feldspar (CL). **(h)** Garnet porphyroblast with inclusions of quartz surrounded by a thin film of K-feldspar. Garnet is partially corroded by sillimanite + quartz (asterisk) (CL). **(i)** Detail of a kyanite crystal rimmed by a plagioclase + biotite corona, in turn partially corroded by sillimanite + quartz (asterisks) (CL).

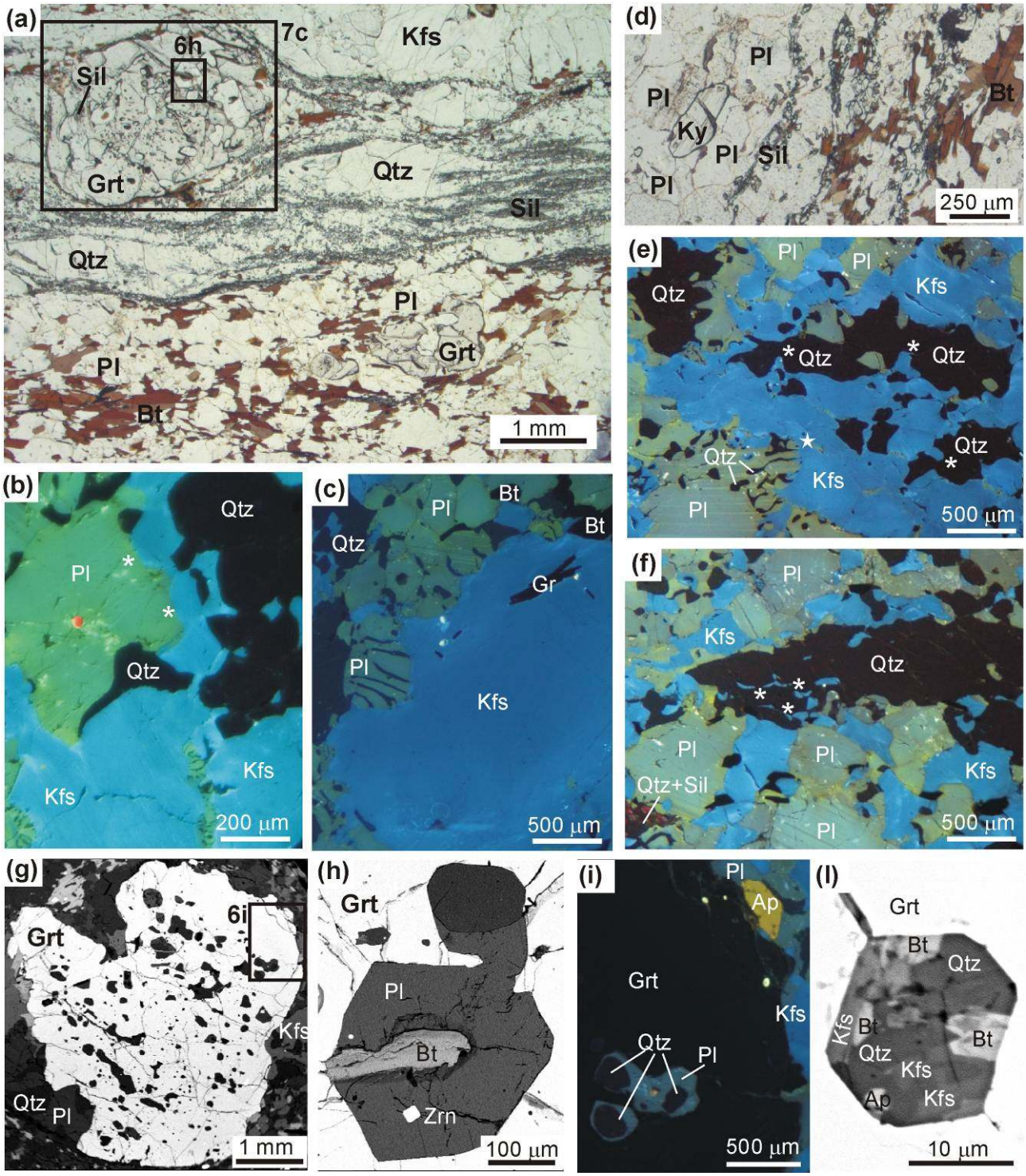

Fig. 5 – Representative microstructures of sample 07-35. **(a)** Garnet porphyroblasts enveloped by the main foliation defined by thin biotite + plagioclase (bottom) or sillimanite + quartz (top) layers, alternating with quartzofeldspathic layers (PPL). **(b)** Detail of a plagioclase crystal from the coarse-grained domains, partially corroded by K-feldspar (asterisks). Note the cuspate shape of quartz in the centre of the microphoto (CL). **(c)** Detail of a fine-grained biotite + plagioclase + quartz domain (top left) partially corroding a large K-feldspar of the coarse-grained domain (CL). **(d)** Detail of a kyanite relict rimmed by a thick corona of plagioclase (PPL). **(e, f)** CL images showing textural relationships between quartz, K-feldspar and plagioclase. In the coarse-grained domains quartz occurs as ribbons partially corroded by K-feldspar (asterisks). K-feldspar is in turn replaced by plagioclase + quartz (myrmekite) of the fine-grained domains (stars). **(g)** Garnet porphyroblast with very small inclusions in the core and large polymineralic inclusions in the rim (Back

Scattered Electron image, BSE). **(h)** Detail of a large polymineralic inclusion in the garnet rim. It consists of corroded quartz and biotite surrounded by plagioclase. Garnet shows crystal faces toward plagioclase (BSE). **(i)** CL image showing a detail of a thick plagioclase film surrounding quartz inclusions in garnet rim. Note the crystal faces of garnet toward plagioclase and the large apatite crystal in the top right portion of the microphoto. **(l)** BSE image of a very small polymineralic inclusion in garnet core, interpreted as a "nanogranite". This inclusion has a negative crystal shape and mainly consists of K-feldspar, quartz and biotite.

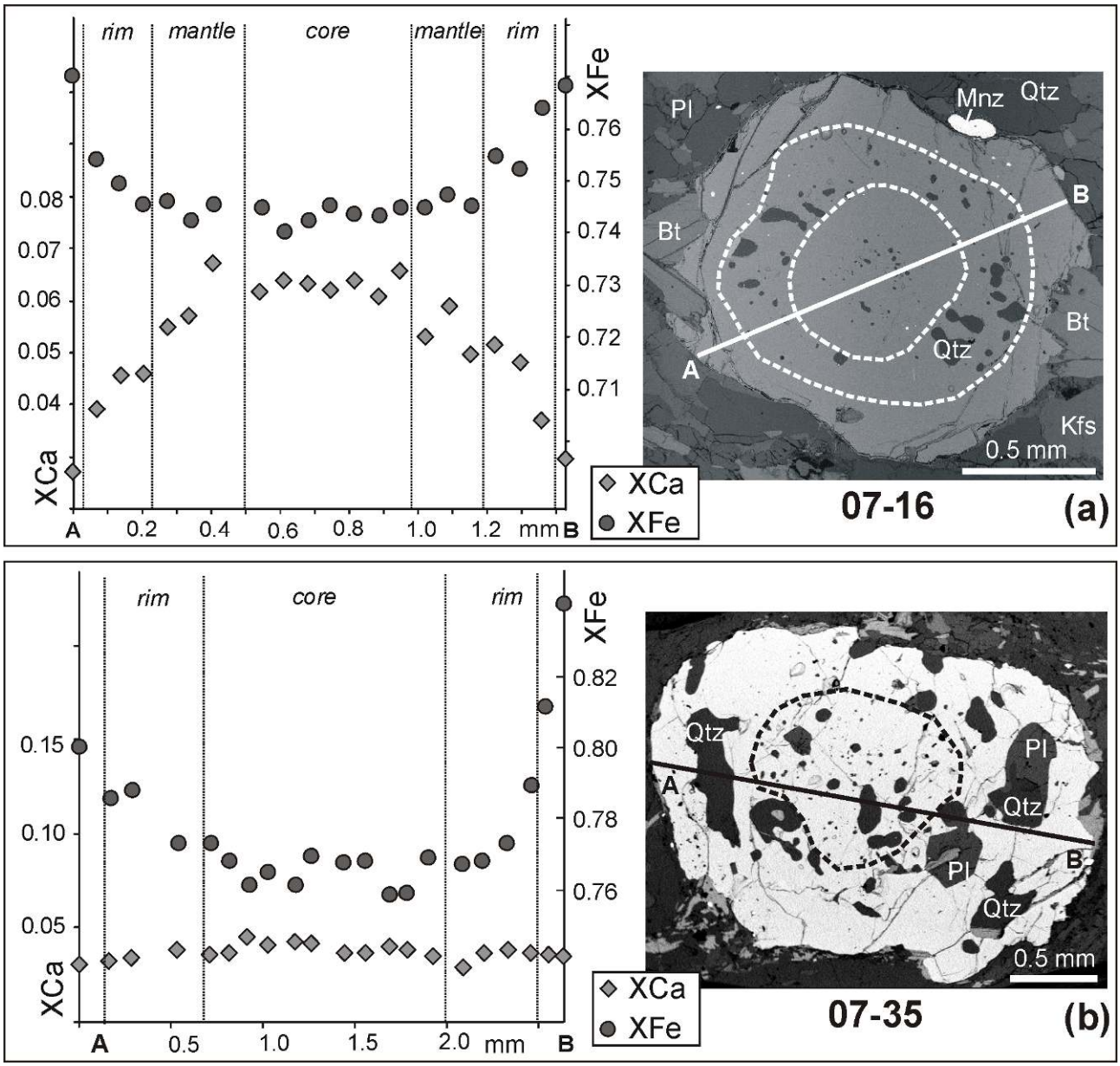

Fig. 6 – Compositional profiles of garnet porphyroblasts [X_{Ca}=Ca/(Ca+Mg+Mn+Fe); X_{Fe}=Fe/(Fe+Mg)] from samples 07-16 (a) and 07-35 (b). The analysed garnet porphyroblasts (BSE images on the right) are the same as in Fig. 4a and 5a, respectively. Dashed lines in the BSE images define the different garnet domains (core-mantle-rim in 07-16, core-rim in 07-35). Garnet from sample 07-35 is representative of porphyroblasts without high-Ca domains.

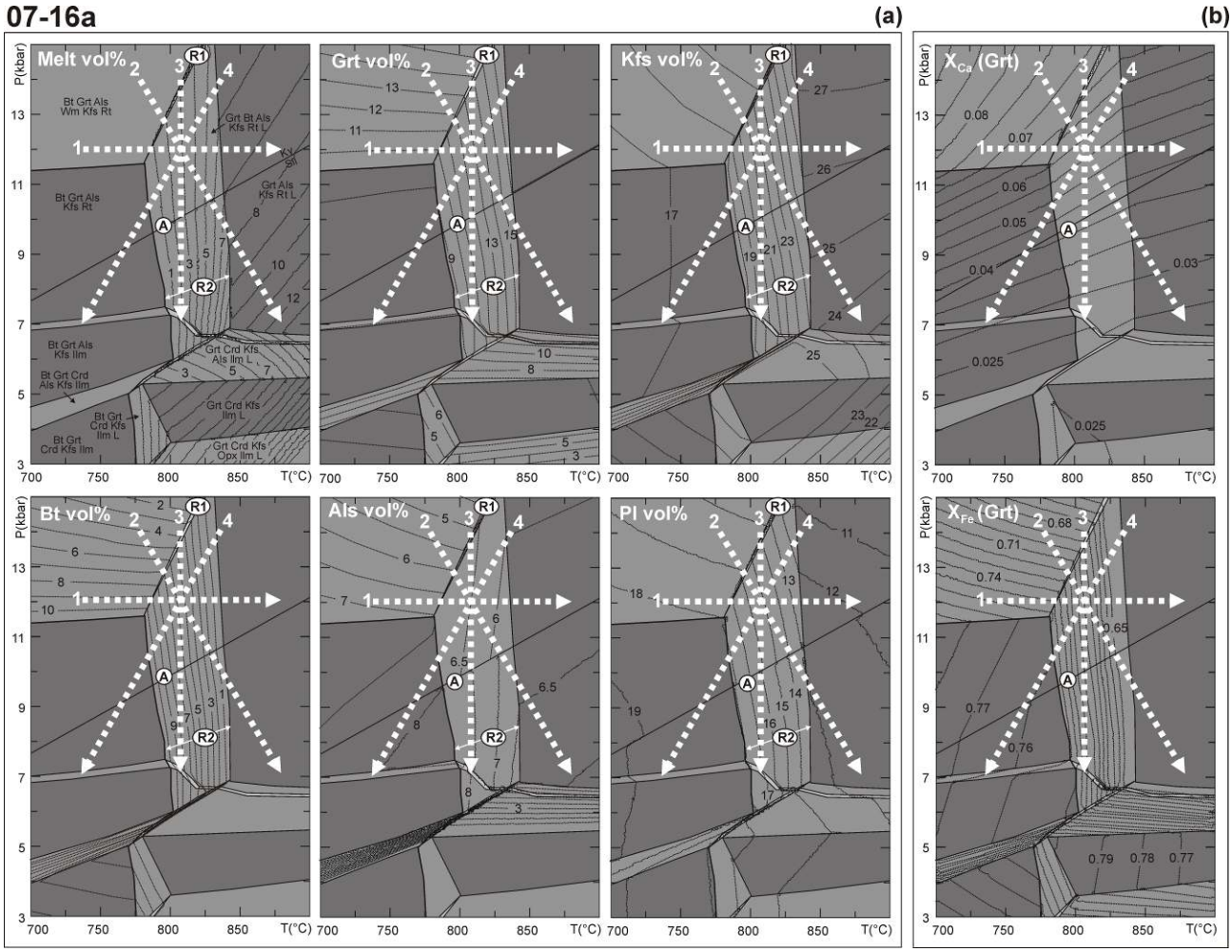

Fig. 7 – P-T pseudosections for sample 07-16 in the MnNKCFMASTH system, calculated using the measured bulk composition 07-16a (Table 2). Light-, medium-, dark- and very dark-grey fields are tri-, quadri-, and penta- and esa-variant fields, respectively. The thick line represents the *solidus* of the system. The assemblage melt + Grt + Bt + Kfs + Pl + Als + Qtz + Rt is shown as field A. Reactions R1 (white mica de-hydration melting) and R2 (biotite de-hydration melting) are indicated. The pseudosections are contoured for vol% of melt, garnet, K-feldspar, biotite, Al-silicates and plagioclase, and for compositional isopleths of garnet (X_{Ca} and X_{Fe}). The four ideal P-T trajectories discussed in the text are also reported (1: isobaric heating; 2: heating-decompression; 3: isothermal-decompression; 4: cooling-decompression).

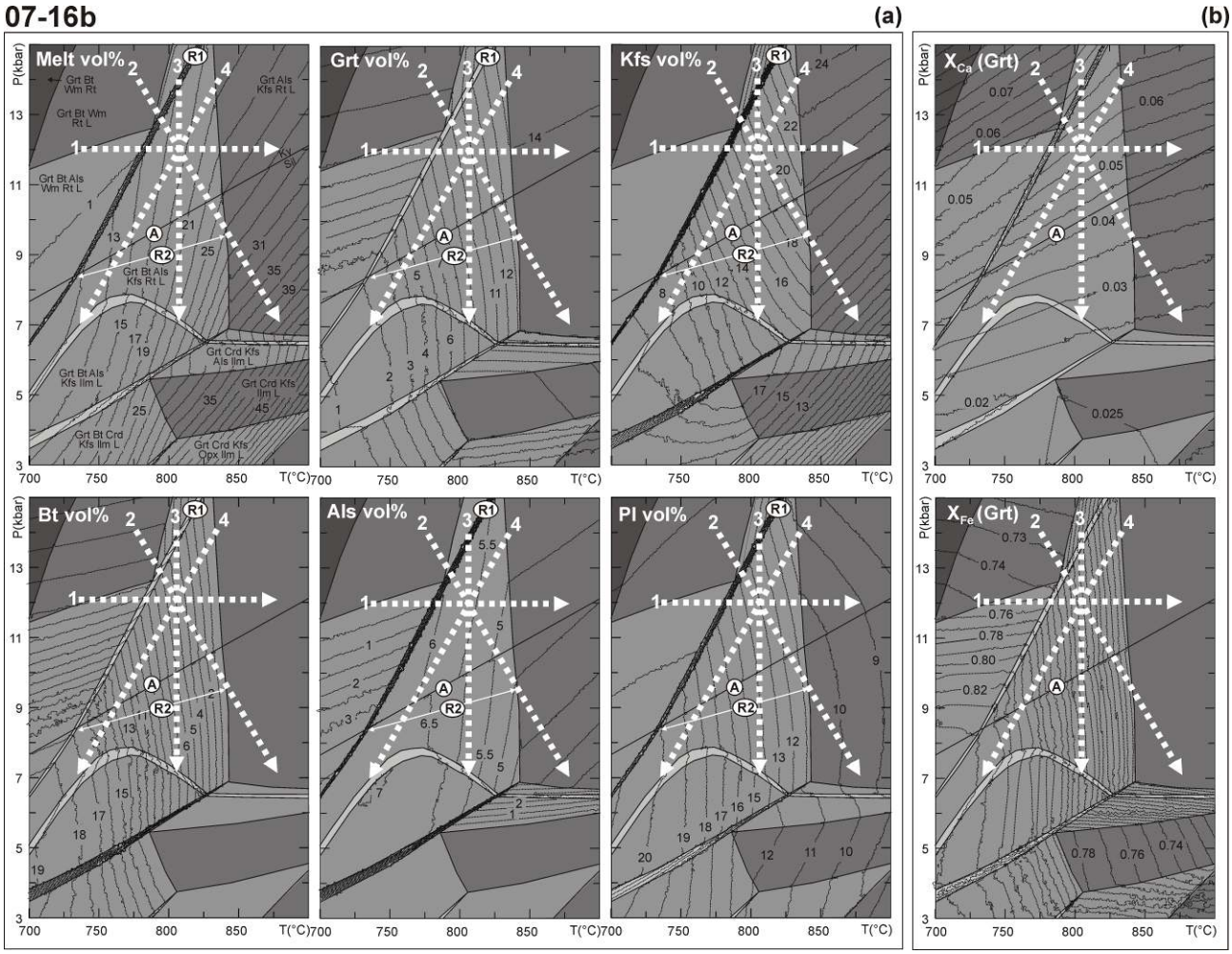

Fig. 8 – P-T pseudosection for sample 07-16 calculated using the melt-reintegrated bulk composition 07-16b (Table 2) obtained from re-integration of 15 mol% of melt (see the Appendix for further details). The *solidus* of the system is at T<670°C (not shown in this figure). Field ig. 7.A and reactions R1 and R2 are the same as in Fig. 7. The pseudosections are contoured for vol% of melt, garnet, K-feldspar, biotite, Al-silicates and plagioclase, and for compositional isopleths of garnet (X_{Ca} and X_{Fe}). The four ideal P-T trajectories are the same as in Fig. 7.

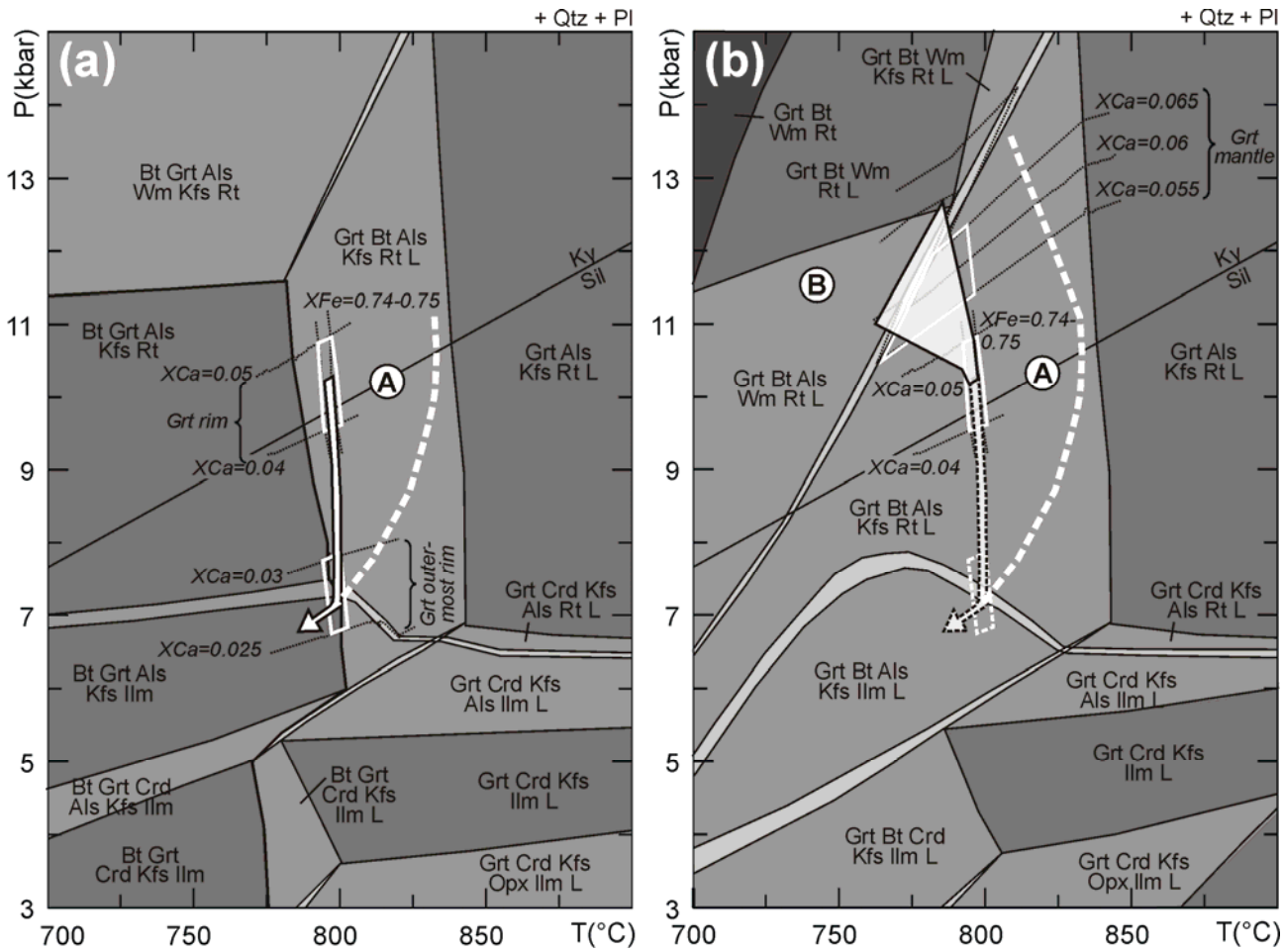

Fig. 9 – (a) P-T pseudosections of Fig. 7 (measured bulk composition 07-16a, Table 2). Peak assemblage (melt + Grt + Bt + Kfs + Pl + Als + Qtz + Rt) is shown as field A. White boxes constrain the P-T conditions of final melt crystallization (white box at lower P) and the peak P_{min}-T_{min} conditions (white box at higher P) as inferred from mineral isomodes (Fig. SM3, available as Supplementary Material) and compositional isopleths of garnet rim (X_{Ca} and X_{Fe}), reported as dotted lines. The dashed arrow is an alternative P-T path which takes in account the possibility that peak P-T conditions were higher than those actually suggested by garnet X_{Ca} and X_{Fe} isopleths (P_{max} and T_{max}). The entire set of isopleths is available at Fig. SM3 available as Supplementary Material. Wm abbreviation indicates a muscovite-like white mica. (b) P-T pseudosection of Fig. 8 (melt-reintegrated bulk composition 07-16b, Table 2). White dashed boxes at low and middle pressure are the same as in (a). The white box at higher-P constrains the approximate P-T conditions for the growth of garnet mantle as inferred from compositional isopleths of garnet (see text and Fig. SM4 for further discussion). The dashed arrow is an alternative P-T path which takes in account the possibility that peak P-T conditions were higher than those actually suggested by garnet X_{Ca} and X_{Fe} isopleths.

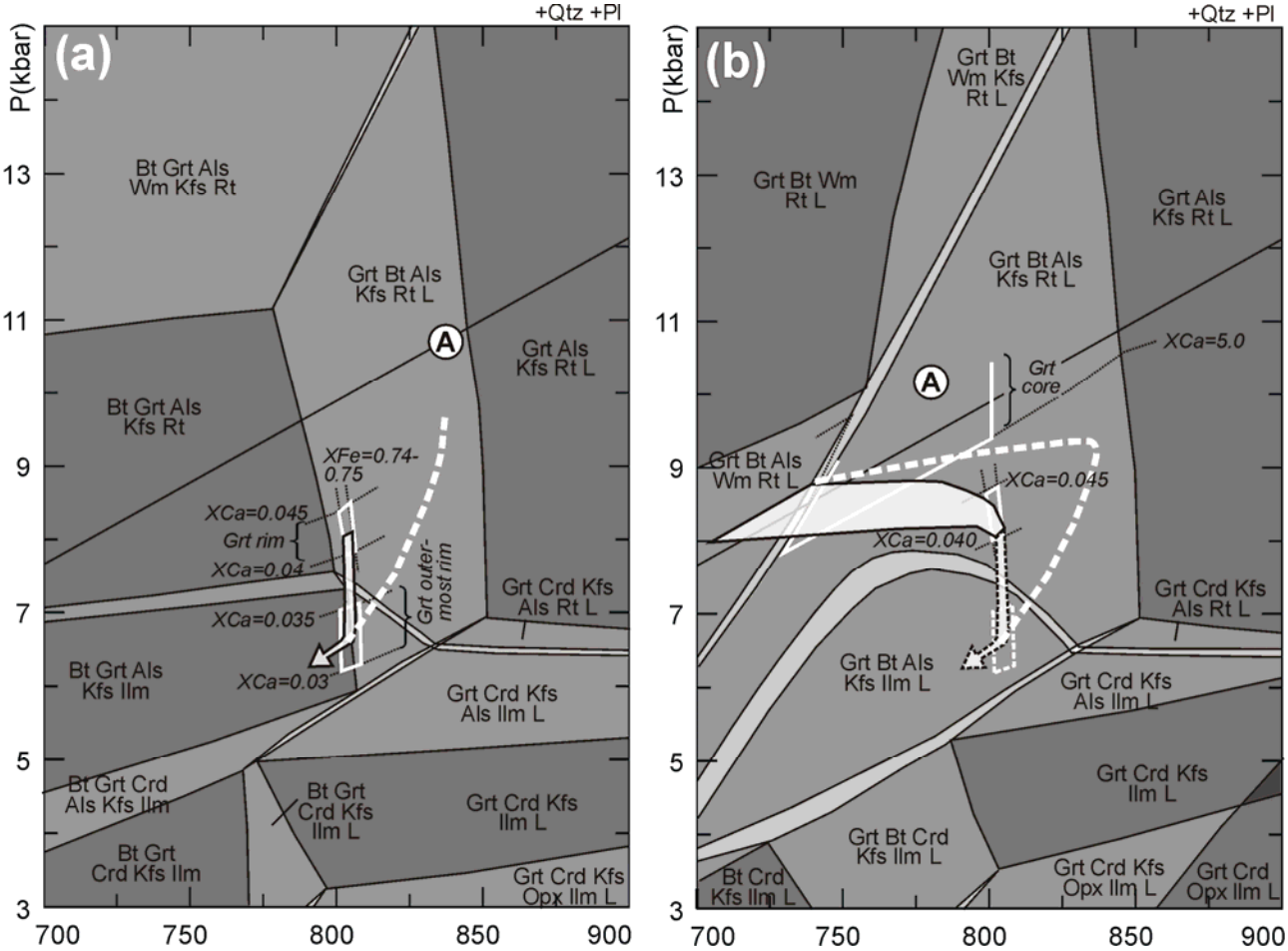

Fig. 10 – (a) P-T pseudosection for sample 07-35 in the MnNKCFMASTH system, calculated using the measured bulk composition 07-35a (Table 2). Light-, medium-, dark- and very dark-grey fields are tri-, quadri-, and penta- and esa-variant fields, respectively. The thick line represents the *solidus* of the system. Peak assemblage (melt + Grt + Bt + Kfs + Pl + Als + Qtz + Rt) is shown as field A. White boxes constrain the P-T conditions of final melt crystallization (white box at lower P) and the peak P_{min}-T_{min} conditions, corresponding to the growth of garnet rim (white box at higher P) as inferred from mineral isomodes (Fig. SM5, available as Supplementary Material) and compositional isopleths of garnet (X_{Ca} and X_{Fe}), reported as dotted lines. The dashed arrow is an alternative P-T path which takes in account the possibility that peak P-T conditions were higher than those actually suggested by garnet X_{Ca} and X_{Fe} isopleths (P_{max} and T_{max}). The entire set of isopleths is available at Fig. SM5,. Wm abbreviation indicates a muscovite-like white mica. (b) P-T pseudosection for sample 07-35 calculated using the melt-reintegrated bulk composition 07-35b (Table 2). The *solidus* of the system is at T<670°C (not shown in this figure). White boxes at low and middle pressure are the same as in (a). The white box at higher-P constrains the approximate P-T conditions for the growth of garnet core as inferred from compositional isopleths of garnet (see Fig. SM6 and text for further discussion). The dashed arrow is an alternative P-T path which takes in account the possibility that peak P-T conditions were higher than those actually suggested by garnet X_{Ca} and X_{Fe} isopleths.

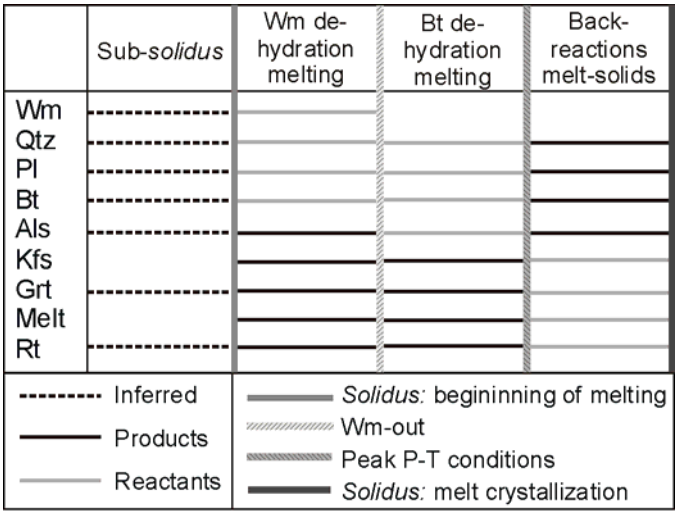

Fig. 11 – Crystallization-event diagram for the studied samples 07-16 and 07-35.

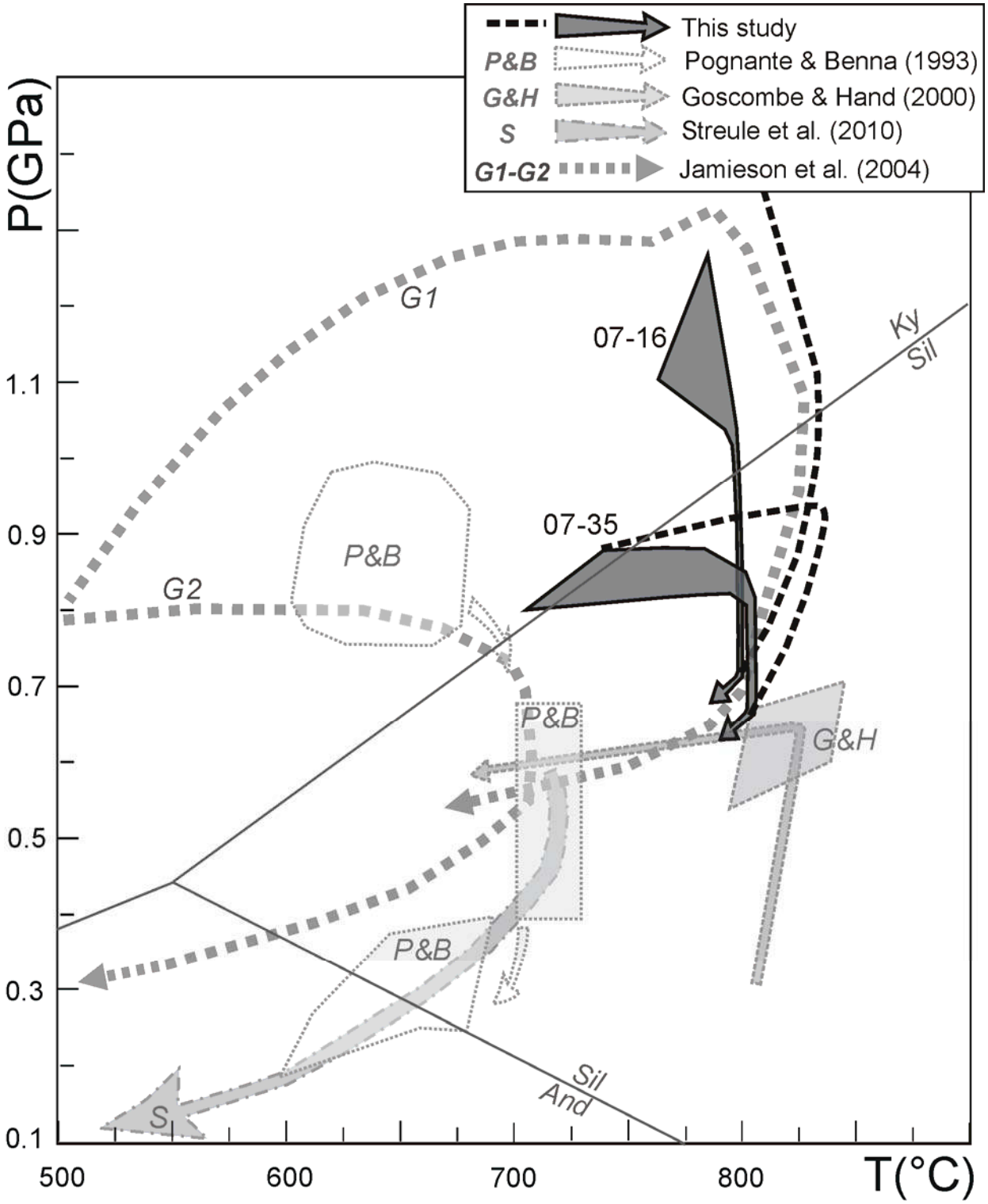

Fig. 12 – P-T diagram showing the P-T paths calculated for the studied samples 07-16 and 07-35 compared with those proposed for the Barun Gneiss by Pognante & Benna (1993), Goscombe & Hand (2000) and Streule *et al.* (2010). The P-T paths predicted by the "channel flow" model (Jamieson *et al.*, 2004) for those rocks that were entrained within the cannel (sample G1) and those that flow outwards with the underlying channel (sample G2) are also reported as dotted arrows for comparison.

Table 1. Representative SEM-EDS analyses of garnet, biotite and feldspars

Sample	**07-16**									
	Garnet				Biotite			Plagioclase		K-feldspar
Anal.	7.8	7.5	7.19	7.1	5.28	3.26		7.25	1.3	6.2
	core	mantle	rim	outer rim	matrix	sympl		matrix	sympl	matrix
SiO_2	37.68	37.96	37.61	37.24	35.51	36.26		63.67	62.75	65.03
TiO_2	b.d.l.	b.d.l.	b.d.l.	b.d.l.	4.11	3.12		b.d.l.	b.d.l.	b.d.l.
Al_2O_3	20.99	21.10	21.48	20.73	17.87	19.02		23.01	23.37	18.71
FeO	31.03	31.94	32.07	33.32	17.786	16.621		b.d.l.	b.d.l.	b.d.l.
MnO	1.24	1.28	1.22	1.53	b.d.l.	b.d.l.		b.d.l.	b.d.l.	b.d.l.
MgO	6.43	6.08	5.91	5.56	10.44	11.82		b.d.l.	b.d.l.	b.d.l.
CaO	2.28	2.00	1.73	0.98	b.d.l.	b.d.l.		4.27	5.26	b.d.l.
Na_2O	b.d.l.	b.d.l.	b.d.l.	b.d.l.	b.d.l.	b.d.l.		8.97	8.71	1.43
K_2O	b.d.l.	b.d.l.	b.d.l.	b.d.l.	9.33	9.06		b.d.l.	b.d.l.	14.86
Total	99.83	100.51	100.14	99.53	95.38	96.16		99.92	100.09	100.03
Si	2.971	2.982	2.966	2.974	2.668	2.675		2.823	2.781	2.988
Ti	b.d.l.	b.d.l.	b.d.l.	b.d.l.	0.232	0.173		b.d.l.	b.d.l.	b.d.l.
Al	1.951	1.954	1.996	1.951	1.582	1.654		1.203	1.221	1.013
Fe^{+3}	0.107	0.082	0.071	0.101	0.189	0.144		b.d.l.	b.d.l.	b.d.l.
Fe^{+2}	1.940	2.017	2.044	2.125	0.928	0.882		b.d.l.	b.d.l.	b.d.l.
Mn	0.083	0.086	0.081	0.104	b.d.l.	b.d.l.		b.d.l.	b.d.l.	b.d.l.
Mg	0.756	0.712	0.695	0.662	1.169	1.300		b.d.l.	b.d.l.	b.d.l.
Ca	0.193	0.168	0.146	0.084	b.d.l.	b.d.l.		0.203	0.250	b.d.l.
Na	b.d.l.	b.d.l.	b.d.l.	b.d.l.	b.d.l.	b.d.l.		0.771	0.749	0.127
K	b.d.l.	b.d.l.	b.d.l.	b.d.l.	0.894	0.853		b.d.l.	b.d.l.	0.871
XCa	0.063	0.055	0.048	0.027			Ab	0.792	0.750	0.128
XFe	0.729	0.746	0.752	0.770	0.489	0.441	An	0.208	0.250	0.000
							Or	0.000	0.000	0.872

Sample	**07-35**									
	Garnet				Biotite			Plagioclase		K-feldspar
Anal.	5.14	5.2	5.29	7.23	4.28	7.27		5.60	5.35	4.29
	core	rim	Ca-rim	outer rim	matrix	inclus.		matrix	inclus.	matrix
SiO_2	38.04	38.27	37.78	37.35	35.64	37.81		61.82	58.31	65.12
TiO_2	b.d.l.	b.d.l.	b.d.l.	b.d.l.	5.25	1.88		b.d.l.	b.d.l.	b.d.l.
Al_2O_3	21.52	21.30	21.41	21.29	18.08	20.05		24.38	26.29	19.07
FeO	32.85	32.70	30.24	35.76	17.61	13.47		b.d.l.	b.d.l.	b.d.l.
MnO	1.16	0.84	0.95	1.41	b.d.l.	b.d.l.		b.d.l.	b.d.l.	b.d.l.
MgO	6.10	6.24	4.25	3.81	10.01	14.61		b.d.l.	b.d.l.	b.d.l.
CaO	1.85	1.47	5.87	1.25	b.d.l.	b.d.l.		5.42	8.49	b.d.l.
Na_2O	b.d.l.	b.d.l.	b.d.l.	b.d.l.	b.d.l.	b.d.l.		8.33	6.80	1.52
K_2O	b.d.l.	b.d.l.	b.d.l.	b.d.l.	9.03	9.54		0.36	0.41	14.78
Total	101.70	100.91	100.63	100.97	96.12	97.36		100.31	100.29	100.49
Si	2.957	2.993	2.971	2.971	2.641	2.720		2.736	2.601	2.976
Ti	b.d.l.	b.d.l.	b.d.l.	b.d.l.	0.293	0.102		b.d.l.	b.d.l.	b.d.l.
Al	1.971	1.963	1.984	1.996	1.579	1.700		1.272	1.382	1.027
Fe^{+3}	0.115	0.052	0.073	0.061	0.287	0.000		b.d.l.	b.d.l.	b.d.l.
Fe^{+2}	2.020	2.087	1.915	2.318	0.803	0.810		b.d.l.	b.d.l.	b.d.l.
Mn	0.076	0.056	0.063	0.095	b.d.l.	b.d.l.		b.d.l.	b.d.l.	b.d.l.
Mg	0.707	0.727	0.499	0.452	1.105	1.567		b.d.l.	b.d.l.	b.d.l.
Ca	0.154	0.123	0.494	0.106	b.d.l.	b.d.l.		0.257	0.406	b.d.l.
Na	b.d.l.	b.d.l.	b.d.l.	b.d.l.	b.d.l.	b.d.l.		0.715	0.588	0.135
K	b.d.l.	b.d.l.	b.d.l.	b.d.l.	0.853	0.875		0.020	0.023	0.862
XCa	0.050	0.040	0.162	0.035			Ab	0.720	0.579	0.135
XFe	0.751	0.746	0.800	0.840	0.497	0.341	An	0.259	0.399	0.000
							Or	0.020	0.023	0.865

Table 2 - Bulk compositions

Sample 07-16						
	Bulk (granulitic assemblage)		Melt reintegrated (790°C, 11kbar)		Bulk after reintegration of 0.15 mol% of melt (approximate protolith)	
	07-16a				*07-16b*	
	mol%	wt%	mol%	wt%	mol%	wt%
SiO_2	72.32	66.84	59.04	66.83	70.59	66.83
TiO_2	0.69	0.85	0.00	0.00	0.60	0.76
Al_2O_3	11.09	17.39	7.49	14.39	10.62	17.07
FeO	5.55	6.13	0.00	0.00	4.83	5.46
MnO	0.15	0.16	0.00	0.00	0.13	0.15
MgO	3.34	2.07	0.00	0.00	2.90	1.84
CaO	1.17	1.01	0.40	0.43	1.07	0.95
Na_2O	2.08	1.98	3.95	4.61	2.32	2.27
K_2O	2.19	3.17	2.69	4.78	2.26	3.35
H_2O	1.42	0.39	26.42	8.97	4.68	1.33
	100.00	99.99	100.00	100.00	100.00	100.00

Sample 07-35						
	BulK (granulitic assemblage)		Melt reintegrated (790°C, 11kbar)		Bulk after reintegration of 0.16 mol% of melt (approximate protolith)	
	07-35a				*07-35b*	
	mol%	wt%	mol%	wt%	mol%	wt%
SiO_2	79.45	74.58	59.04	66.83	76.63	73.67
TiO_2	0.57	0.71	0.00	0.00	0.49	0.63
Al_2O_3	8.60	13.70	7.49	14.39	8.45	13.78
FeO	3.49	3.92	0.00	0.00	3.01	3.46
MnO	0.06	0.07	0.00	0.00	0.05	0.06
MgO	2.18	1.37	0.00	0.00	1.88	1.21
CaO	1.11	0.97	0.40	0.43	1.01	0.91
Na_2O	1.50	1.45	3.95	4.61	1.84	1.82
K_2O	2.00	2.94	2.69	4.78	2.10	3.16
H_2O	1.04	0.29	26.42	8.97	4.54	1.31
	100.00	100.00	100.00	100.00	100.00	100.00

Table 3 - Measured vs.modelled modes

	07-16		07-35	
vol%	meas.	800°C, 7 kbar mod.	meas.	800°C, 6 kbar mod.
Qtz	37.4	37.5	51.7	51.4
Pl	20.6	18.2	14.7	13.6
Kfs	14.5	17.5	14.3	16.8
Bt	12.1	10.8	9.2	7.8
Grt	8.5	7.8	4.8	4.1
Ky/Sil	6.7	7.7	5.1	5.9
Rt/Ilm	0.2	0.6	0.1	0.5
Total	100.0	100.0	100.0	100.0